Astronomy & Astrophysics manuscript no. output March 11, 2019
(DOI: will be inserted by hand later)

Detecting shocked intergalactic gas with X-ray and radio observations

F. Vazza[1,2,3], S. Ettori[4,5], M. Roncarelli[1,4], M. Angelinelli[1], M. Brüggen[2], C. Gheller[6]

[1] Dipartimento di Fisica e Astronomia, Universitá di Bologna, Via Gobetti 93/2, 40122, Bologna, Italy
[2] Hamburger Sternwarte, Gojenbergsweg 112, 21029 Hamburg, Germany
[3] Istituto di Radioastronomia, INAF, Via Gobetti 101, 40122, Bologna, Italy
[4] INAF, Osservatorio di Astrofisica e Scienza dello Spazio, via Pietro Gobetti 93/3, 40129 Bologna, Italy
[5] INFN, Sezione di Bologna, viale Berti Pichat 6/2, I-40127 Bologna, Italy
[6] Swiss Plasma Center, EPFL, SB SPC Station 13 - 1015 Lausanne, Switzerland

Accepted ???. Received ???; in original form ???

Abstract. Detecting the thermal and non-thermal emission from the shocked cosmic gas surrounding large-scale structures represents a challenge for observations, as well as a unique window into the physics of the warm-hot interagalactic medium. In this work, we present synthetic radio and X-ray surveys of large cosmological simulations, in order to assess the chances of jointly detecting the cosmic web in both frequency ranges. We then propose best observing strategies tailored for existing (LOFAR, MWA and XMM) or future instruments (SKA-LOW and SKA-MID, *Athena* and eROSITA). We find that the most promising targets are the extreme peripheries of galaxy clusters in an earlier merging stage, in which ongoing merger triggers the fast compression of warm-hot gas onto the virial region of galaxy clusters. By taking advantage from earlier detection in the radio band, future deep X-ray integrations will have the chance to study of such elusive gas phase *in emission*, and to study plasma conditions in the dynamic warm-hot intergalactic medium with unprecedented detail.

Key words. galaxy clusters, ICM

1. Introduction

Since decades, numerical simulations (e.g. Cen & Ostriker, 1999; Davé et al., 2001; Gheller et al., 2016; Martizzi et al., 2018) have shown that the most important mass component of the baryons in the cosmic web is the elusive Warm-Hot Intergalatic Medium (WHIM), a rarefied gas phase with densities $\mathrm{n} \sim 10^{-5} - 10^{-4}$ part/cm^3 and temperatures $\mathrm{T} \sim 10^5 - 10^7$K.

The WHIM should fill the volume within cosmic filaments as well as in the outskirts of galaxy clusters, and attain its temperature via strong ($\mathcal{M} \gg 10$) accretion shocks.

Detections of absorption lines through the WHIM of intracluster filaments have been claimed (e.g. Werner et al., 2008; Nicastro et al., 2010). More recently, Nicastro et al. (2018) reported the high significance detection of two OVII absorbers in the X-ray spectrum of a quasar at $z \geq 0.4$, possibly tracing the WHIM.

In a few nearby galaxy clusters and limited to few narrow sectors, the thermodynamical properties of the intracluster medium have been mapped with X-ray observations out to R_{100} (e.g. Simionescu et al., 2011; Urban et al., 2011). Others mapped the gas properties in concentric rings out to R_{200} by combining X-ray and SZ data (Ghirardini et al., 2019; Ettori et al., 2019; Eckert et al., 2019). The terminal parts of five massive filaments connected to the massive cluster A2744 have recently been observed with XMM-Newton (Eckert et al., 2015), possibly representing the first imaging ever of cosmic filaments in the X-ray band, which made it possible to estimate that $5 - 10\%$ of the mass fraction of missing baryons may be contained by such objects.

Moreover, the study of the Sunyaev-Zeldovich effect from the outer region of clusters, either in single pointings of interacting clusters (Planck Collaboration et al., 2013; Bonjean et al., 2018) or in stacked observations of larger samples (de Graaff et al., 2017; Tanimura et al., 2018) has detected the hot ($\sim 10^7$ K) and very overdense ($\sim 10 - 10^2 \rho/\langle\rho\rangle$) gas component, potentially contributing to $\sim 10 - 50\%$ of missing cosmic baryons.

Cosmological hydrodynamical simulations have shown that the WHIM is well traced by the underlying galaxy distribution (see, e.g., Nevalainen et al., 2015) and that its diffuse emission is responsible for a significant fraction of the unresolved X-ray background in very deep Chandra exposures (see Roncarelli et al., 2006b; Hickox & Markevitch, 2007), with a predicted surface brightness of the order of $1 - 5 \cdot 10^{13}$erg/(cm^2 s deg^2) in the $\sim 0.5 - 1$ keV energy band, with uncertainties related to its metal composition

Send offprint requests to: E-mail: franco.vazza2@unibo.it

(Ursino et al., 2010; Cen & Chisari, 2011; Roncarelli et al., 2012). However, the systematic detection and characterisation of single WHIM systems remain a challenge due to its low emissivity. Hence, efforts have focused on stacking and statistical studies on the (auto)correlation function of its X-ray signal (see, e.g., Piro et al., 2009; Takei et al., 2011; Ursino et al., 2011; Cappelluti et al., 2012; Kolodzig et al., 2018).

The planned X-ray mission *Athena* X-ray observatory [1], expected to be launched by $\sim$ 2030, holds great promise to detect the WHIM in absorption. Among its ambitious goals, *Athena* aims to trace the missing baryons in the intergalactic medium via detecting their absorption lines, through the emission of bright sources up to $z \sim 2$. It is expected that in total ~ 80 sources can be studied at the highest possible resolution for spectroscopic studies with the instrument X-IFO studies ($\Delta E = 2.5$ eV) (Barcons et al., 2012). The limitation of this technique is that, of course, most of these sources are unpredictable and variable, and only a dozen of bright enough sources per year may be detected to study filaments.

In this work, we wish to explore the complementary approach, in which *Athena* detects the WHIM in emission.

Planelles et al. (2018) have recently presented detailed radiative transfer simulations of the X-ray emission from a cluster at $z \approx 0.3$, reporting that the emission from the WHIM phase only accounts for the $\sim 5\%$ in the [0.5-2] keV band and $\sim 1\%$ in the [2-10] keV band. In general, the WHIM is found to have a more filamentary structure than the $\geq 10^7$ K gas phase, extending several Mpc out from the virial regions of galaxy clusters. Using a larger volume with the Illustris-TNG suite, Martizzi et al. (2018) recently studied the WHIM properties from $z = 4$ to $z = 0$, confirming that most of that filaments are more baryon-rich than the cosmic average, but that they have a significantly lower metallicity than the ICM, which makes their observability via X-ray observations challenging.

Luckily for observations, in addition to the X-ray window, also the radio window is suitable for the imaging of the cosmic web, thanks to the current (e.g. LOFAR, MWA, ASKAP, MEERKAT) and future (e.g. the Square Kilometer Array) generations of large radio telescopes. Theoretical works have shown that filaments of the cosmic web should be surrounded by strong and quasi-stationary accretion shocks (e.g. Ryu et al., 2003; Pfrommer et al., 2006; Vazza et al., 2011), at which a tiny fraction of relativistic electrons may be accelerated. This is similar to what occurs in radio relics or cluster radio shocks at the periphery of clusters (e.g. Hoeft & Brüggen, 2007; Wittor et al., 2017; van Weeren et al., 2019).

A few radio observations have already claimed the detection of diffuse synchrotron emission from the shocked gas at the interface between galaxy clusters and filaments attached to them (Bagchi et al., 2002; Giovannini et al., 2010; Farnsworth et al., 2013; Vacca et al., 2018). Moreover, the Faraday Rotation signature of filamentary accretions on the Coma cluster has been claimed (Bonafede et al., 2013). Recently, the signature in Faraday space of filaments overlapping to the emission of a $z = 0.34$ radio galaxy has been claimed by O'Sullivan et al. (2018), while the detection of faint diffuse radio emission at the interface of pre-merger galaxy clusters has been reported using LOFAR-HBA by Botteon et al. (2018) and Govoni et al. (submitted).

Simulations have shown that the low surface brightness ($\leq \mu$Jy/arcsec^2 at ~ 100 MHz), highly polarised ($\sim 70\%$) and large angular scale ($\geq 1^\circ$) emission that is expected to be produced by the shocked cosmic web (e.g. Keshet et al., 2004; Brown, 2011; Vazza et al., 2015b) makes the low-frequency radio spectrum ($\nu \leq 300$ MHz) is the most suitable for a detection, owing to the typically superior sampling of short baselines in low-frequency radio telescopes. In particular, the radio continuum surveys of SKA-LOW should detect parts of the magnetic cosmic web, with statistics depending on the (unknown) details of particle acceleration and magnetic field distribution in such rarefied plasma (e.g. Vazza et al., 2015a,b, 2017a). Additional to this, also polarisation surveys with the SKA-MID may be able to detect the Faraday Rotation signal from the terminal part of filaments connected to massive galaxy clusters, provided that a large statistics of polarised sources is available (Locatelli et al., 2018).

The exciting possibility of detecting both *thermal* and *non-thermal* emissions from the cosmic web with joined X-ray and radio surveys is the subject of this work. In a pilot study for the "SKA-Athena Synergy White Paper" (Cassano et al. 2018, Sec. 5.2.1) we first investigated the potential for a synergy between SKA and *Athena* in the study of the rarefied cosmic web. Our first results suggest that cluster outskirts are promising targets, with a small but non-negligible fraction of the cosmic web that might be detectable by both instruments (working at their nominal maximum capabilities). This possibility will make it possible to perform WHIM science with *Athena* not only limited to absorption lines towards high-z powerful sources, but also on a few, carefully selected objects. Based on these first results, in this work we use one of the largest cosmological magneto-hydrodynamical simulation ever produced to better assess to which extent can future X-ray and radio observations constrain the physical properties of the WHIM, taking into account the performances of X-ray and radio telescopes under realistic observing conditions.

The structure of the paper is as follows: in Sec. 2 we introduce our simulations, and in particular in Sec. 2.2 we introduce our methods to produce sky models of our simulated universes. In Sec. 3 we present our results for the intrinsic emission properties of the simulated cosmic web in X-ray and radio bands, while in Sec. 3.3.3 we specifically investigate mock *Athena* and SKA observations of our fields, and in Sec. 3.3.4 we present a preliminary simulation of future spectroscopic analysis with X-IFU. Physical and numerical limitations of our results are given in Sec. 4 while our conclusions are given in Sec. 5.

[1] http://www.the-athena-x-ray-observatory.eu

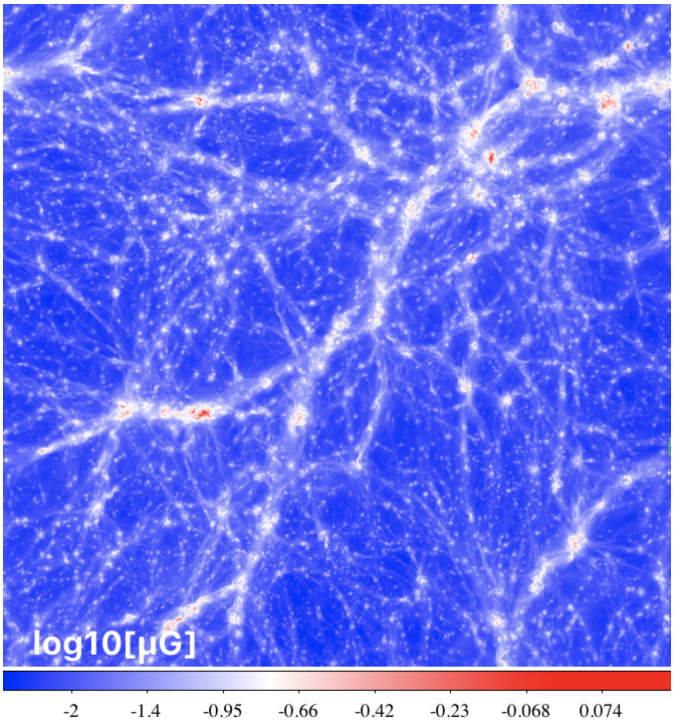

Fig. 1: Projected (mass weighted) magnetic field strength at $z = 0.05$ for our simulated 100^3 Mpc^3 volume.

2. Methods

2.1. Cosmological simulations

As in previous work (Vazza et al., 2017a, 2018a), we simulated a comoving 100^3Mpc^3 box with a uniform grid of 2400^3 cells and 2400^3 Dark Matter particles, using the cosmological MHD code ENZO [2] (Bryan et al., 2014). The fixed (comoving) spatial resolution of this run is $\Delta x = 41.6$ kpc/cell while the fixed Dark Matter mass resolution is $m_{\rm dm} = 8.62 \cdot 10^6 M_{\odot}$ per particle. We initialized magnetic fields at $z = 45$ as a simple uniform background of of $B_0 = 0.1$nG (one order-of-magnitude below the upper limits on primordial magnetic fields from the analysis of the CMB, Ade et al. 2015), and we used the MHD method of Dedner (Dedner et al., 2002), ported to GPUs (Wang et al., 2010) to evolve magnetic fields at run-time.

Our run is non-radiative and does not include any treatment for star formation or feedback from active galactic nuclei. To a first approximation, these processes are not very relevant for the radio and X-ray properties of the peripheral regions of galaxy clusters and filaments, which are our main focus (see Sec. 4 for a discussion).

We assumed a ΛCDM cosmological model, with density parameters $\Omega_{\rm BM} = 0.0455$, $\Omega_{\rm DM} = 0.2265$ (BM and DM indicating the baryonic and the dark matter respectively), $\Omega_{\Lambda} = 0.728$, and a Hubble constant $H_0 = 70.2$ km/(sec Mpc). In Sec.3.3.4 we will also present results for the resimulation of a massive galaxy clusters with the same setup, but using nested initial conditions and Adaptive Mesh Refinement (8 levels) to achieve a higher resolution ($\Delta x_8 \approx 4$ kpc/cell), similar to Vazza et al. (2018b).

An impression of the three-dimensional distribution of magnetic fields in our simulation (which is one of the biggest MHD simulations ever performed in cosmology) is given in Fig.1, and shows the variety of magnetic field strength and configurations that are found across cosmic environments at $z = 0.05$.

2.2. Sky models

2.2.1. X-ray emission

For the X-ray emission, we assumed for simplicity a single temperature and a single (constant) composition for every cell in the simulation, and we compute the emissivity from the B-APEC emission model [3], assuming ionization equilibrium and including continuum and line emission.

We consider a *constant* metallicity across the volume, $Z/Z_{\odot} = 0.3$ (see a discussion in Sec. 4 for the rather small impact of metallicity in most of our estimates).

For each energy band, we compute the cell's X-ray emissivity, $S_X = n_H n_e \Lambda(T, Z) dV$, where n_H and n_e are the number density of hydrogen and electrons (assuming a primordial composition) respectively, and dV is the constant volume of our cells.

We do not include the additional contribution from the Inverse Compton emission from the same relativistic electrons accelerated by shocks and responsible for the radio emission (see next Section), whose amplitude depends on the assumed electron energy distribution at low-energies (e.g. Bartels et al., 2015). However, our estimates show that the Inverse Compton in the [0.8-1.2] keV band is negligible ($\leq 1\%$) compared to the thermal emission of the cluster. It may start to dominate only at very large radii, $\geq 2 - 3R_{100}$, at which no detection seems to be feasible with realistic exposure times.

The left panel of Fig. 2 shows the integrated X-ray emission from the simulated box located at at $z = 0.05$, in the [0.8-1.2] keV energy band. At the angular distance corresponding to this redshift ($D_A \approx 201.6$Mpc) this volume covers $28.4^{\circ} \times 28.4^{\circ}$. For reference, *Athena*'s Wide Field Imager field of view is $\sim 40' \times 40'$, while X-IFU's field of view is $\sim 5' \times 5'$.

2.2.2. Radio

We predict the synchrotron radio emission assuming that diffusive shock acceleration (DSA, e.g. Kang et al. 2012 and references therein) is able to accelerate a very small fraction of thermal electrons swept by shocks up to relativistic energies ($\gamma \geq 10^3 - 10^4$), and that the intergalactic medium has a non-negligible magnetic field, as suggested by our MHD simulation (e.g. Fig.1). As in previous work (Vazza et al., 2015b), we identify shocks in the simulation in post-processing with a velocity-based approach, and we compute the radio emission from electrons accelerated in the shock downstream following Hoeft & Brüggen (2007). The typical efficiency (ξ_e)

[2] www.enzo-project.org

[3] https://heasarc.gsfc.nasa.gov/xanadu/xspec/manual/Models.html

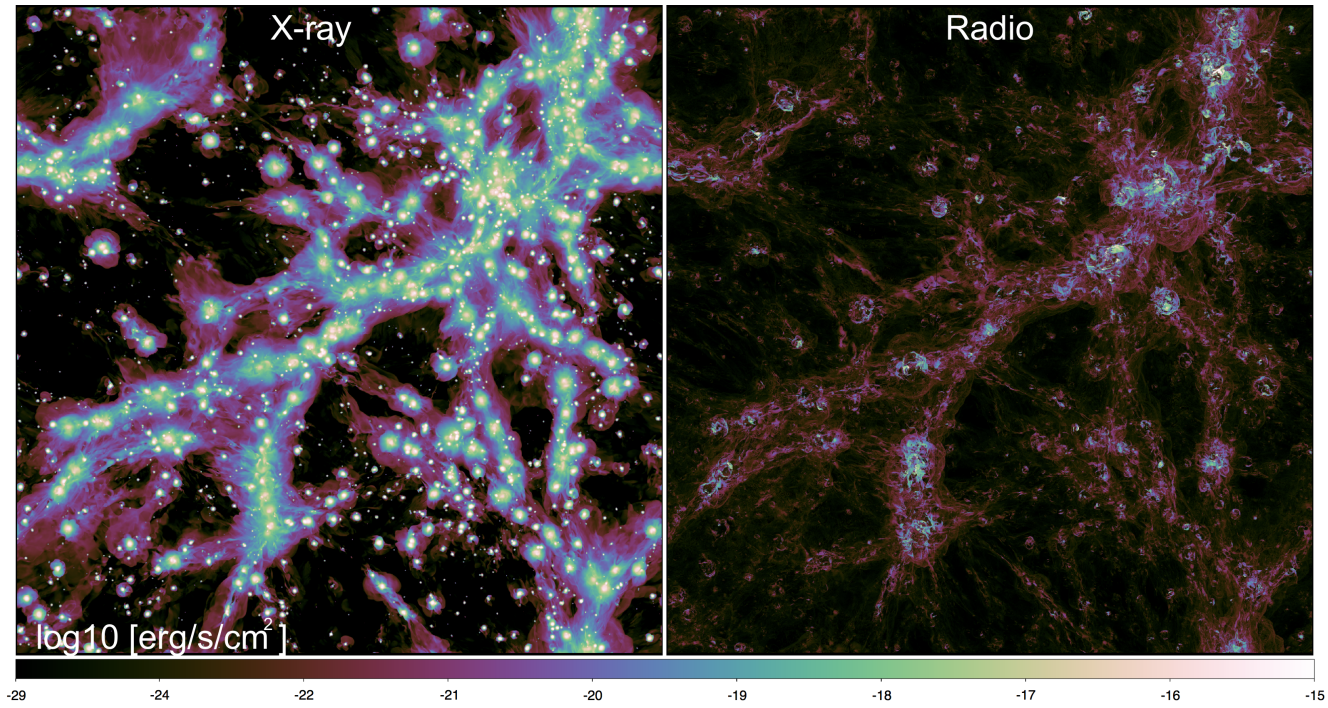

Fig. 2: Projected X-ray emission in the [0.8-1.2] keV band (left) and mock radio emission at 260 MHz (right) for our 100^3 Mpc^3 volume located at $z \approx 0.05$.

considered in the conversion efficiency from shock kinetic energy into the energy of relativistic electrons is small and it scales with the Mach number and the upstream gas temperature as in Hoeft & Brüggen (2007): for example it is $\xi_e \approx 10^{-6}$ for $\mathcal{M} = 3$ shocks in a $T = 10^7$K, and $\xi_e \approx 6 \cdot 10^{-4}$ for $\mathcal{M} \geq 50$ shocks with a $T = 10^5$K. The additional (possible) role of shock obliquity (e.g. Wittor et al., 2017) and of fossil reaccelerated electrons (e.g. Pinzke et al., 2013) is neglected here for simplicity; we caution however that the additional presence of fossil electrons in cluster outskirts and in filaments will increase our estimates here, at least limited to $\mathcal{M} \leq 3-4$ shocks in the simulation (while for stronger shocks the direct injection from DSA should dominate the emission in any case). The downstream radio emission is the convolution of the several power-law distributions of electrons which overlap in the cooling region, to which we assign the integrated radio spectrum of $I(\nu) \propto \nu^{-s}$, where $s = (p-1)/2 + 1/2$, with $p = 2(\mathcal{M}^2+1)/(\mathcal{M}^2-1)$.

An example of the radio emission at $\nu = 260$ MHz from our simulation is given in Fig. 2. The SKA-LOW primary beam at this frequency should be of order $\sim 5^\circ \times 5^\circ$, while our sky model covers $28.4^\circ \times 28.4^\circ$. The radio emission is clearly more diffuse compared to the X-ray emission, because unlike the latter it does not scale (only) with gas density, but with the shock kinetic power, which can be significant in cluster outskirts (e.g. Ryu et al., 2003). The fact that the radio power typically extends out to larger cluster radii makes it a very good probe of the rarefied cosmic web, but at the same time reduces the chances of overlap with X-ray detections, as we shall see in the next Section, with a sweet spot on the scale of cluster outskirts.

3. Results

3.1. X-ray emission and radio emission from the cosmic web

We start by computing the X-ray emission from the entire simulation, as a function of environment and for different energy ranges, namely [0.3-0.8], [0.8-1.2], [1.2-2.0], [2.0-5.0] an [5.0-7.0] keV, assuming $Z = 0.3 Z_\odot$ everywhere. In Fig. 3 we show the median and total X-ray emission from all pixels in the sky model of Fig.2, binned as a function of their gas temperature, which is mass-weighted along the entire line-of-sight [4].

At $T_{\rm mw} \leq 5 \cdot 10^6$ K, the X-ray emission from the WHIM is always highest in the softest band (0.3-0.8 keV). Most of the emission is free-free radiation above $T_{\rm mw} \geq 10^6$ K, while at lower temperatures emission lines get dominant. In the entire [0.3-1.2] keV part of the spectrum at these temperatures lines are dominant, and they are $\sim$ 10 times more than in the other higher bands (see Sec.4 for variations in the assumed metallicity of our gas). Conversely, for $T_{\rm mw} \geq 10^7$K, the X-ray emission is always more prominent in the [2.0-5.0] keV band, all contributed by free-free emission.

This suggests that, in principle, the [0.3-0.8] keV band has the highest chances of detecting the WHIM in emission. However, when the full response of *Athena* is taken into account, as well as the realistic contribution from astrophysical and instrumental backgrounds, the [0.8-1.2] keV band gives a

[4] It is important to notice here that the *average* temperature values along a line of sight of 100 Mpc underestimate by a factor $\sim$ 10 (or more) the real temperature values in 3D.

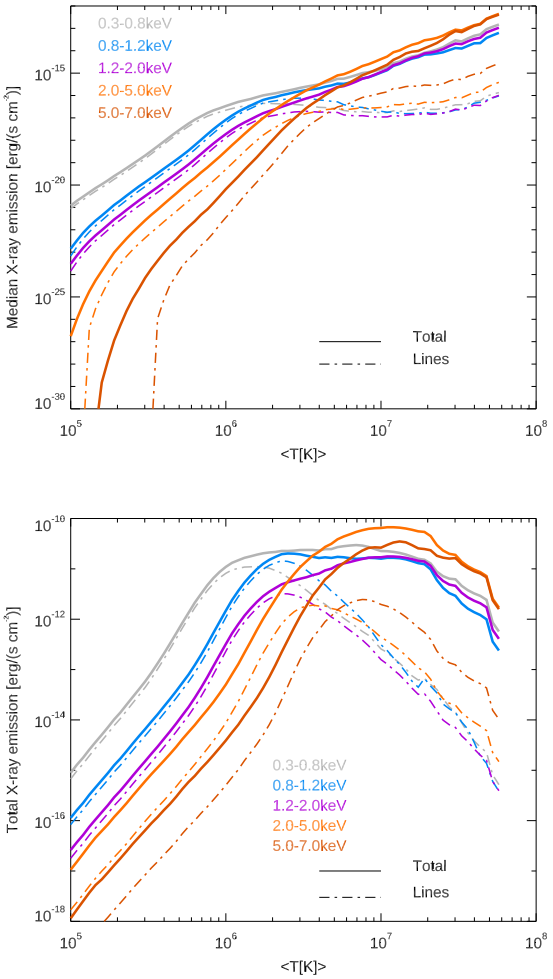

Fig. 3: Distribution function of the median X-ray emission (top) and of the total X-ray emission (bottom) for different energy ranges, as a function of the projected mass-weighted temperature of gas in our simulation. The solid lines give the total X-ray emission, while the dot-dashed lines give the contribution only by line emission (assuming a fixed 0.3 $Z_{\odot}$ metallicity everywhere).

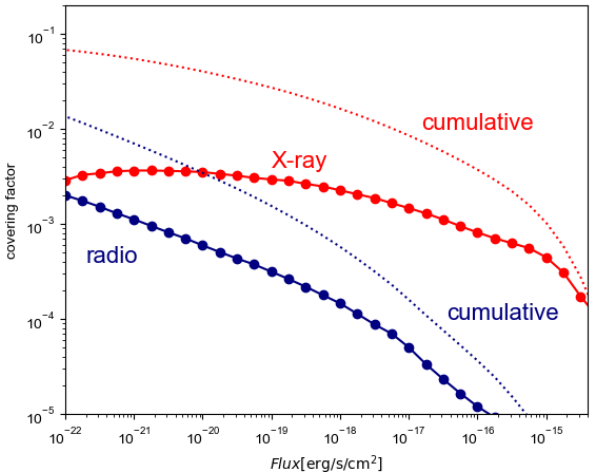

Fig. 4: Area coverage as a function of X-ray and radio flux (in the [0.8-1.2] keV range and at 260 MHz, respectively) for the same sky models of Fig.5. The solid lines give the differential distribution while the dashed line give the cumulative.

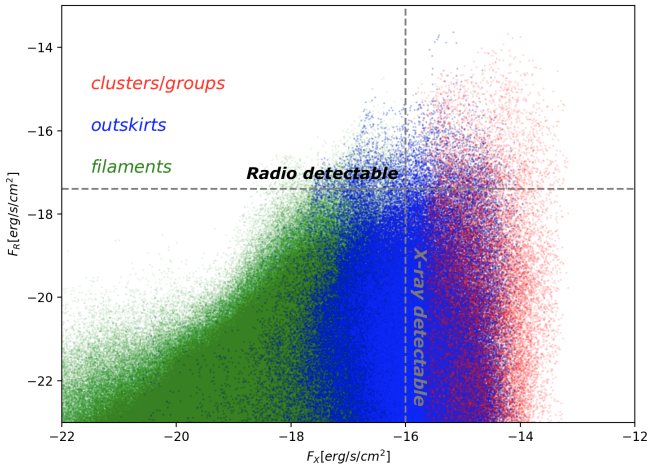

Fig. 5: Distribution of X-ray and radio flux for all simulated pixels in our sky model (Fig.2), by color-coding the pixels located within different structures. The additional grey lines roughly delimit the regions which will become observable with future X-ray and radio observations.

significantly higher chances of detection. In Sec.3.3 we will show in detail how our modelling suggests the above finding, which stems from a quantitative comparison of the fraction of pixels tracing various environments across our simulation, which can be detected as a function of exposure time and energy bands for different instruments. While we defer to that Section for the demonstration of this finding, we anticipate this result here in order to present more general trends found in our data, limiting for simplicity to the [0.8-1.2] keV band in particular.

Second, we characterized the distribution of X-ray and radio emission from the simulated cosmic web, by comparing the X-ray signal in the [0.8-1.2] keV range to the radio emission at 260 MHz. In Figure 4 we show the cumulative and differential distribution of X-ray, F_X and radio flux, F_R, for the pixels in Fig. 2, in which no observational cuts are taken into account for now. While both distribution shows a similar decreased power-law behaviour, the radio distribution has a steeper behaviour for increasing F_R, indicating the relative scarcity of powerful detectable radio emission from cluster shocks (e.g. radio relics). Considering that $\approx 10^{-17}$ erg/s/cm^2 is the fiducial value for the future sensitivity of SKA-LOW at this frequency, from this plot we can derive that at most a $\sim 1\%$ of the entire radio emission produced by the cosmic web will be detectable even in the future. Due to the flatter slope of the F_X distribution, for a fiducial detection threshold of $\approx 10^{-16}$ erg/s/cm^2 we have instead that a $\sim 10\%$ of the total thermal emission from the cosmic web in this energy range may be detectable (assuming

observations at high galactic latitudes and long exposures). We will comment more on this issue in Sec. 5.

By computing the distribution of F_R as a function of F_X for the pixels in our simulated sky model (Fig. 5), we can demonstrate the lack of a simple relation between the two emission mechanisms. For a given bin in X-ray flux the radio emission can vary by more than 6 orders of magnitude. Interestingly, we measure that the distribution of F_R in the volume peaks for 10^{-17} erg/s/cm^2 $\leq$ F$_{\rm X}$ $\leq 10^{-14}$ erg/s/cm^2 , i.e. of the order the sensitivity level of *Athena*.

The pixels in this range of F_X are mostly related to the external accretion regions of galaxy clusters and groups, as shown by the different color-coding adopted in Fig. 5, in which we marked pixels as belonging to clusters or groups in red if they fall within the projected volume ($\leq R_{100}$) of halos. Those that are at a projected distance $R_{100} \leq r \leq 3 \cdot R_{100}$ from halos centres are marked in blue. Finally, pixels were marked in green if they belong to filaments, i.e. if they have a projected gas density in the range $1 \leq n_{\rm proj}/\langle n \rangle \leq 50$ and have a projected temperature in the range 10^5 K $\leq$ T$_{\rm mw}$ $\leq 10^7$ K.

As shown by the additional approximate detection limit for future X-ray and radio observations ($\sim 10^{-16}$ erg/s/cm^2 for [0.8-1.2] keV and $4 \cdot 10^{-18}$ erg/s/cm^2 for 260 MHz , dashed lines in Fig.5), for the majority of our simulated pixels $F_X \gg F_R$, i.e. the X-ray emission outshines the radio emission. The few noticeable exceptions are the spikes in the radio flux, marked by the vertical stripes in the plot. They are mostly related to projected temperatures of $T_{\rm mw} \sim 10^6 - 10^7$ K. The visual inspection shows that such patterns are associated with structure formation shocks, often in the periphery of galaxy clusters or in between merging cluster pairs, and we will focus on them in the next section.

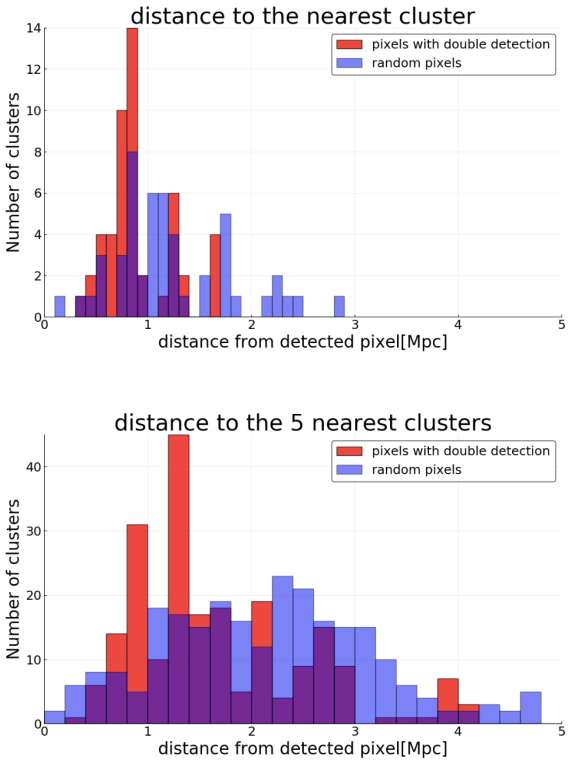

Fig. 6: Distribution function of average (projected) distance to the 1st and ot the 5th nearest cluster from the location of "double detections" in our simulated dataset. The blue data are for the distances computed from a randomly drawn set of position in our maps, for a number of points equal to our "double detections".

3.2. Enhanced gas emission from cluster outskirts

In this section we wish to identify the most promising targets for a joint detection of the WHIM in the radio and in the X-ray band. To this end, we computed the clustering and morphological properties of massive halos found in the neighborhood pixels that are detected in the X-rays and in radio emission.

Our 100^3 Mpc^3 simulation box contains a total of 2347 halos with $M_{100} \geq 10^{12} M_\odot$, 268 halos with $M_{100} \geq 10^{13} M_\odot$ and 26 halos with $M_{100} \geq 10^{14} M_\odot$ at $z = 0$, consistent with the expected mass function (e.g. Sheth & Tormen, 1999) within the limits of a Poissonian statistics. We first measured the distribution of distances of halos from each jointly detectable pixel, and in Figs. 6 we give the example of the (projected) distance to the 1st and to the 5th nearest halo. In Fig. 7 we show the radial distribution of halos around such jointly detected pixels. To quantify the excess clustering around such pixels, we also computed distributions for an equal number of randomly drawn positions in the simulation, which represents the background level of clustering.

On average, the pixels which can be detected in radio and X-rays have a higher concentration of halos around them, up to the 10th most distant halos around their location, and at least up a ~ 30 Mpc when $\geq 10^{12} M_\odot$ halos are considered, or up to $\sim 10 - 15$ Mpc if we limit to $\geq 10^{14} M_\odot$ halos.

So how do clusters neighbouring these double detectable regions look like? We explored this by computing the average emission properties of halos at their periphery, to study how their dynamical properties (often associated with the environment) relate to doubly detectable regions.

In the top panel of Fig. 8 we computed the 95th percentile of X-ray and radio emission at R_{100} from our set of clusters, and plot it as a function of the cluster total mass within the same radius. Large symbols mark the objects in which at least a 1% for the area of the R_{100} shell (considering a width 41.6 kpc) can be detected simultaneously in X-ray and in radio, given our assumed detection thresholds. At such large distances, the brightest end of the X-ray emission distribution does not scale with cluster mass, being dominated by rare positive brightness enhancements which are mostly due to the presence of large scale companions (whose amplitude does not directly correlate with the host cluster mass), while the radio emission is overall well correlated with the host cluster mass.

In our model the radio emission is solely caused by shocks, thus the radio power scales with the shock kinetic power, $\Phi_K \propto \rho v_s^3 \sim M_{100}^{3/2}$. Small departures from this relation are due to projection effects, as well as to the non-linear dependence of the acceleration efficiency on the shock Mach number. In the

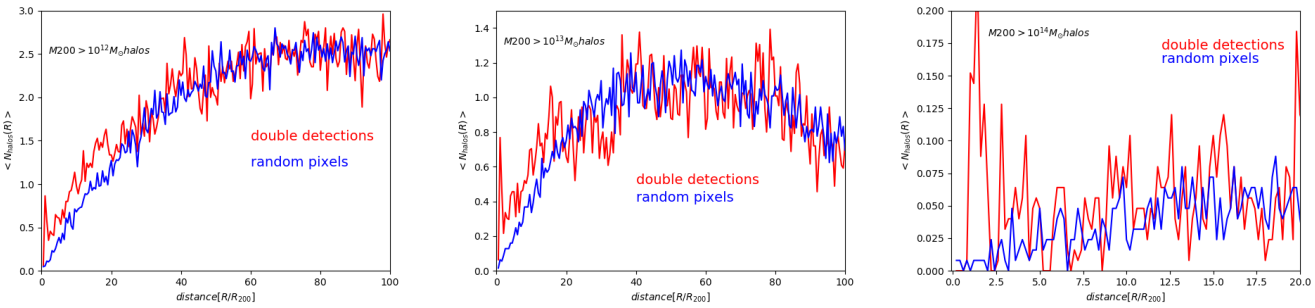

Fig. 7: Average number of clusters (considering a different lower threshold in mass) at a given distance from the location of "double detections" in our simulated dataset. The blue data are for the distances computed from a randomly drawn set of position in our maps, for a number of points equal to our "double detections".

lower panel of Fig. 8 we quantify the detectability of cluster outskirts for each object, by computing the shell fraction that can be observed, as a function of the host cluster mass: the odds of a joint detection of extreme cluster outskirts do not scale with the cluster mass, and joint detections are found across the entire mass range of our sample.

We checked whether the enhanced emission in cluster outskirts correlate with large-scale disturbances in the matter distribution, using the *mass sparsity*, simply defined as the ratio between the total mass enclosed within two different radii, e.g. $S = M_{100}/M_{200}$. While other morphological parameter estimators are useful to characterized the dynamical stage of galaxy clusters in their internal regions, based on X-ray images (e.g. Cassano et al., 2010), the mass sparsity correlates well with cosmological parameters (σ_8 and Ω_M) as well as with the dynamical state of clusters to a larger radius (e.g. Corasaniti et al., 2018), and is a convenient parameter to measure as it involves two integrated quantities (e.g. either the total mass or the integrated X-ray luminosity) which should be robustly probed by future X-ray surveys. However, our search for a dependence between the mass sparsity of our cluster sample and enhanced emission in their outskirts did not highlight any dependence as doubly detectable regions can be found at both large ($S \sim 1.6$) and small ($S \sim 1.1$) values of sparsity.

Next, we analyse the distribution of X-ray and radio emission around our clusters, beginning with the projected radial profile of their emission. In Fig. 9, we show radial distributions of three relevant examples for the average X-ray ([0.8-1.2] keV band) and radio (260 MHz) emission in 2D shells around their respective X-ray peaks. For each object, we show the median profiles (thick lines) as well as the $5-25-75-95\%$ regions around the median. The choice of cutting the profiles for $\geq 95\%$ limits the contribution from X-ray bright gas clumps, which get typically masked in real observations, and are not a good tracers for the ICM/WHIM conditions (e.g. Roncarelli et al., 2006a; Zhuravleva et al., 2011; Eckert et al., 2013). The surface fraction that can be detected in the X-ray or in the radio domain as a function of the angular distance from the cluster centre of the 20 most massive clusters in our sample is given in the right panels of the same figure. For each cluster, the vertical

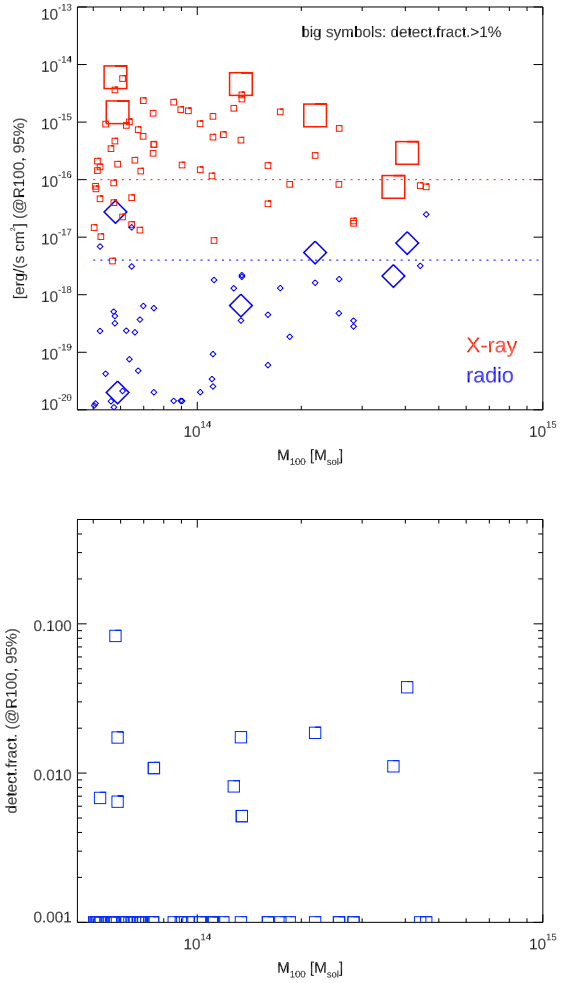

Fig. 8: Top panel: 95th percentile of the X-ray and radio emission from a thin radial shell at R_{100} as a function of the cluster mass, for $\geq 5 \cdot 10^{13} M_{\odot}$ clusters in our simulation at $z = 0.05$. The horizontal lines show the reference detection threshold for both cases. Large symbols corresponds to clusters in which $\geq 1\%$ of the R_{100} shell can be simultaneously detected in X-ray and in radio. Bottom panel: detection fraction for the R_{100} shell in our clusters at $z = 0.05$, considering the simultaneous detection in X-ray and radio, as a function of the cluster mass

axis gives the fraction of the surface that is above the detection threshold in X-ray, in radio, or simultaneously in both.

In roughly half of our sample a significant level of the X-ray emission should be detectable by *Athena* at the projected R_{100} (consistent with Fig.8, which typically corresponds to $\sim 0.4 - 0.6$ degrees from the cluster centre. Conversely, in the radio domain several clusters host detectable radio emission in their innermost regions, which is associated to transient powerful merger shocks, leading to "classic" radio relics (van Weeren et al., 2019). Even with the planned sensitivity of SKA-LOW at 260 MHz, the average radio emission there will be well below the detection threshold in most cases, and only in $\sim 10 - 20\%$ of clusters we expect direct single detection of the shocked WHIM at the virial radius [5], while a detection is guaranteed via stacking techniques (Vazza et al., 2017a).

The second and third clusters shown in Fig. 9 (identified as "F" and "L" in the panels) are most frequent cases: there a non-negligible fraction ($5 - 20\%$) of the R_{100} shell is detectable in X-rays with *Athena*, while in both cases only a very tiny fraction of radio emission would be detectable by SKA-LOW. Moreover, the is no spatial overlap between X-ray and radio detection, hence the *Athena* and SKA will not be able to study the same portion of the ICM/WHIM in these objects, which are the majority in our sample.

However, in the first system ("B" in Fig.9) a $\sim 10\%$ of the R_{100} shell will be detectable in X-ray with *Athena*, as well as a $\sim 5 - 10\%$ in the radio domain, with a non-negligible overlap of detectable regions in the two instruments, offering the chance joint analysis. A striking difference emerges from the X-ray profile, and may offer the key to predict the occurrence of such rare configurations: there is a prominent secondary X-ray emission peak outside of the virial radius of the first cluster, indicating the presence of a massive nearby cluster companion. This is not present in the profile of cluster "L", while a secondary peak is seen in cluster "F" but at a much larger distance from the virial radius of the main cluster.

Systems such as "B" only account for $\sim 10 - 20\%$ of our sample, and they suggest that *the presence of a massive companion, likely in an early interaction stage, is key to producing X-ray detectable bridges that are engulfed by detectable radio emission.*

We suggest that the regions that offer the best chances of detection at $\sim R_{100}$ in X-ray and in radio are parts of the WHIM that resemble the periphery of clusters. As already noticed by other authors (e.g. Roncarelli et al., 2006a; Iapichino et al., 2011) the usage of a too rigid temperature selection to define the WHIM phase, e.g. $T \sim 10^5 - 10^7$ K, does not fully capture the different possible histories of the weakly X-ray emitting gas that may be detected in the periphery of galaxy clusters.

Such bridges are remnants of large-scale filaments once connecting these systems. By the time at which interacting systems have nearly interesting virial regions, the gas flow in between them reaches $\sim 1000 - 2000$ km/s velocities, and this

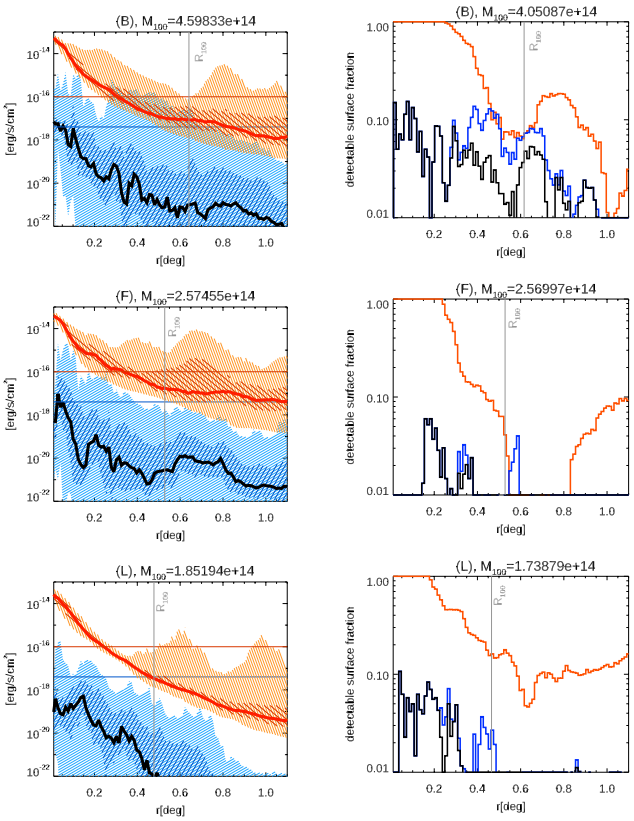

Fig. 9: Left panels: 2D X-ray (in the [0.8-1.2] keV range, in red/orange curves) and radio emission (at 260 MHz, blue curves) profiles for the 3 halos in our volume at $z = 0$, showing the median (thick lines) and the $33 - 66\%$ and $5 - 95\%$ percentile ranges (shaded areas). The horizontal axis gives the angular distance from the centre of each cluster. The horizontal lines gives the reference X-ray (red) and the radio (blue) detection threshold considered in the paper, while the vertical grey lines give the location of R_{100} for each cluster. Right panels: radial profiles of the surface fraction that can be detected in X-ray (red), in radio (blue) or by both (black) for the same objects.

forces their outer gas layers to be significantly compressed. This compression causes a boost of the X-ray emission level, roughly of order $\sim (\rho_2/\rho_1)^{11/4}$ if ρ_2 is the gas density after the compression and ρ_1 was the gas density before the close encounter [6]. Moreover, the increase in gas temperature boosts the chance of detection this tenuous gas phase in the [0.8-1.2] keV, by letting a larger portion of the X-ray emission spectra to "enter" the soft X-ray window. On the other hand, the implied shock velocity are modest, with typical Mach numbers of $\mathcal{M} \leq 5 - 10$, fragmented on $\sim 10^2$ kpc scales. We will analyze in detail one of such systems at higher spatial resolution in Sec.3.3.4.

[5] We notice that here our emission model is more conservative with respect to our previous analysis in Vazza et al. (2017a), in which a 10 times larger initial seed field was assumed.

[6] This follows from considering $L_X \propto \rho^2\sqrt{T}$ and $T \propto \rho^{3/2}$ in the adiabatic case.

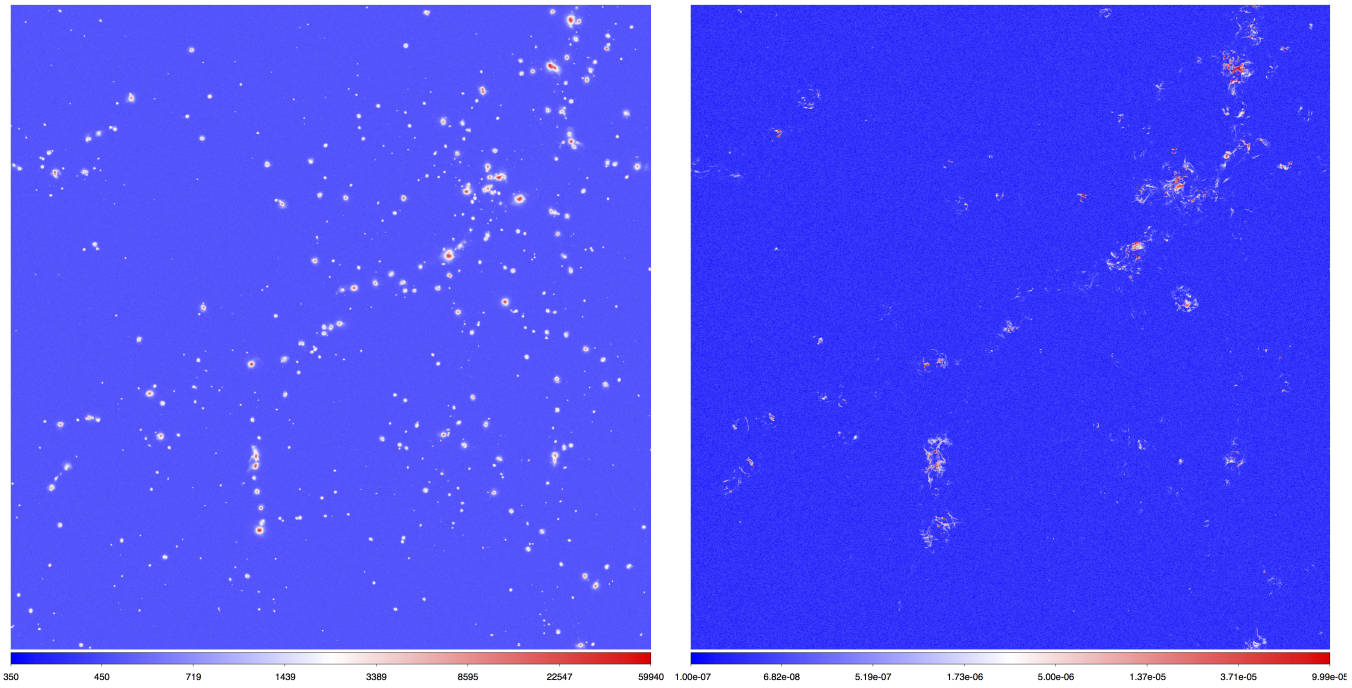

Fig. 10: Mock X-ray (left) and radio (right) observations of the same simulated box of Fig. 1, located at $z \approx 0.05$. The left panel shows the photon counts for a 1 Ms integration in the [0.8-1.2] keV band using WFI (see Sec. 2.2.1 for details) while the right panel gives the result of a mock radio survey at 260 MHz with the SKA-LOW (see Sec. 2.2.2 for details), in units of $[\mathrm{Jy/arcsec^2}]$. Each panel covers $\approx 28.4^\circ \times 28.4^\circ$in the sky. Both images include the noise level expected for the respective instrument, band and integration time (in the case of SKA-LOW, we also consider the confusion noise level).

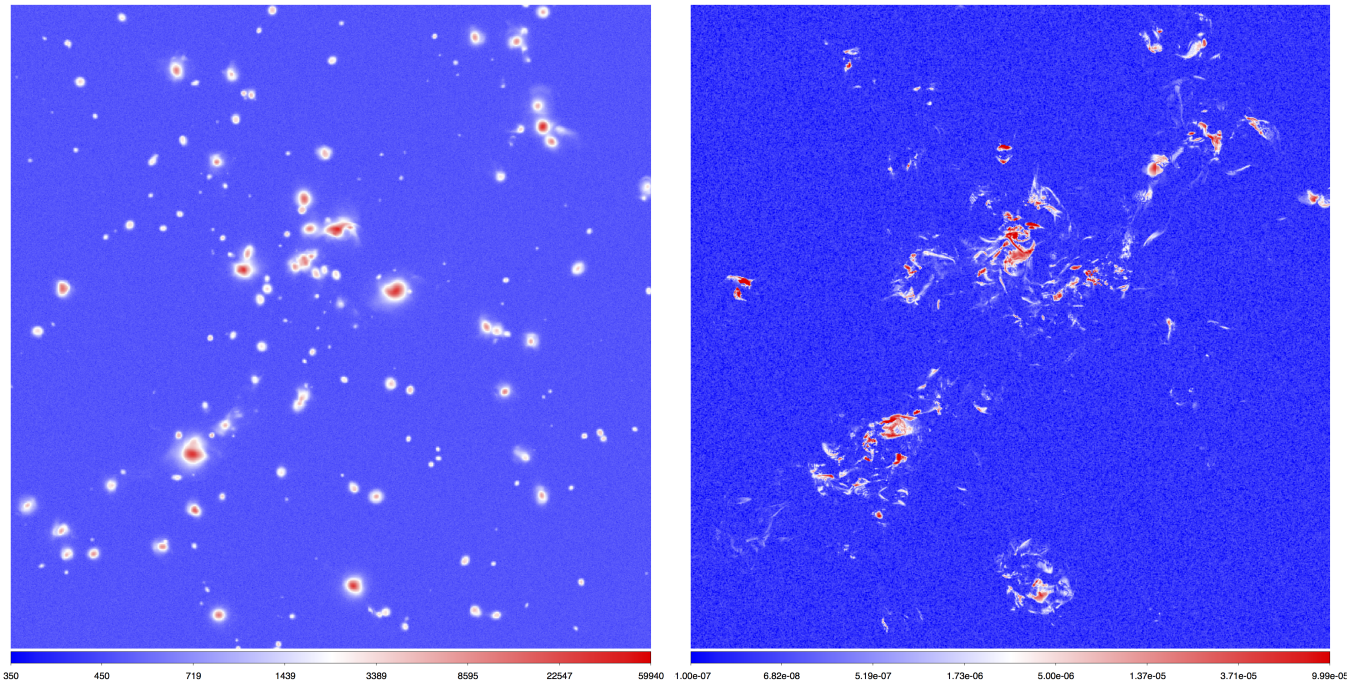

Fig. 11: Close-up view of a crowded $\approx 30 \times 30$ Mpc^2 region of Fig. 2. Each panel covers $\approx 8.5^\circ \times 8.5^\circ$in the sky. As in Fig.10, the left panel gives the photon counts for a 1 Ms integration in the [0.8-1.2] keV band using WFI while the right panel gives the result of a mock radio survey at 260 MHz with the SKA-LOW, in both cases with noise included.

Table 1: Values adopted for our mock X-ray observations with *Athena*, eROSITA and XMM-Newton. For each different energy band we give the count rate due to the effective (sky+instrumental) background, the fraction $f_{\rm abs}$ of source counts un-absorbed by the galactic column density (assuming $n_H = 2 \cdot 10^{20} {\rm cm}^{-2}$), and the mean effective collecting area $A_{\rm eff}$ in that energy range [7].

Instrument	Energy Band [keV]	$B_{\rm bg}$ $\frac{\rm counts}{\rm arcmin^2 Msec}$	$f_{\rm abs}$	$A_{\rm eff}$ [cm^2]
Athena-WFI	0.3-0.8	$2.1 \cdot 10^4$	0.83	9511
	0.8-1.2	$3.1 \cdot 10^3$	0.95	12139
	1.2-2.0	$1.4 \cdot 10^3$	0.98	10841
	2.0-5.0	$3.4 \cdot 10^3$	0.99	4673
	5.0-7.0	$2.0 \cdot 10^3$	1.00	2131
eROSITA	0.3-0.8	$2.2 \cdot 10^3$	0.83	610
	0.8-1.2	$4.6 \cdot 10^2$	0.95	1243
	1.2-2.0	$4.2 \cdot 10^2$	0.98	1267
	2.0-5.0	$4.1 \cdot 10^2$	0.99	287
	5.0-7.0	$3.0 \cdot 10^2$	1.00	88
XMM	0.3-0.8	$4.6 \cdot 10^3$	0.83	1056
(PN + 2MOS)	0.8-1.2	$1.4 \cdot 10^3$	0.95	1655
	1.2-2.0	$1.8 \cdot 10^3$	0.98	1894
	2.0-5.0	$3.4 \cdot 10^3$	0.99	1337
	5.0-7.0	$1.7 \cdot 10^3$	1.00	998

3.3. Synthetic observations

Here we discuss strategies to detect the gas emission located in bridges of close cluster pairs. In order to quantify the detectability of intracluster gas bridges with existing or future observations, we produced a small survey of mock observations in X-ray and radio bands, assuming either the specifications for wide-area surveys of specific instruments, as well as of dedicated reprocessing (e.g. with UV tapering in the radio case) of specific objects in order to increase the sensitivity to diffuse emission.

3.3.1. X-ray: *Athena* , eROSITA and XMM

Here we compared the performances of shallow full-sky surveys with eROSITA (either 1.6 ks in the entire sky or 20 ks in the polar regions), with long targeted exposures with *Athena*'s Wide-Field Imager (1 Ms or 100 ks) and with XMM-Newton (100 ks), for different energy bands.

To quantify the observable regions of each mock observation we use the signal-to-noise ratio (S/N), quantified as:

$$S/N = \frac{f_{\rm abs} \cdot S}{\sqrt{f_{\rm abs}(S + 2B_{\rm bg})}} \quad (1)$$

where S is the number of photon counts originating from the source within a given energy band and collected by the effective area $A_{\rm eff}$, $f_{\rm abs}$ is the ratio between the absorbed (from an assumed galactic column density of $n_{\rm H} = 2 \cdot 10^{20} {\rm cm}^{-2}$) and not absorbed source counts for a typical plasma with gas temperature of 3 keV, metallicity of 0.3 times the solar value, and $B_{\rm bg}$ is the estimated total X-ray background, including the contributions from the Milky Way, the unresolved (20% of the total) cosmic X-ray background and the instrumental background [8]. The details of the mock observing parameters considered here are given in Tab. 1.

The left panels of Fig. 10-11 show the mock X-ray exposure maps of our simulated 100^3 Mpc^3 located at $z = 0.05$ in the [0.8-1.2] keV band, for a 1 Ms exposure in every pixel of the box and considering background counts as in Table 1 for an *Athena*-WFI observation. Extended tails of detectable X-ray emission can often be seen in between closely interacting systems (only a fraction of which corresponds to physically bound objects actually interacting in 3 dimensions).

To quantify the fraction of the gas in the cosmic web which can be detected by each instrument in different bands, it is convenient to measure the typical signal-to-noise that each observing strategy can achieve as a function of the local temperature, which we can parametrise through the mass-weighted mean temperature along the line of sight within each pixel.

Fig. 12 displays the median/maximum S/N for pixels in different environment and for different energy ranges in *Athena*'s WFI integration of 1 Ms. The lower panel in the same Figure shows the detectable fraction of the sky model (marked as $S/N \geq 3$) as a function of temperature. As anticipated in Sec. 3.1.1, the combination of the instrumental and particle background, of the galactic absorption and of the effective collecting area as a function of energy makes the [0.8-1.2]keV slightly better compared to the [0.3-0.8]keV range for a detection of the emission from the baryons in the (projected) gas temperature range $T \geq 10^6 - 10^7$ K, which are more connected to cluster outskirts and cluster-cluster bridges. In this range, we expect that $\sim 40\%$ ($\sim 80\%$) of the gas with projected gas temperature of $\sim 10^6$ K ($\sim 5 \cdot 10^6$ K) can be detected with high significance with a 1Ms integration, respectively. The detection fraction drops to $\sim 20\%$ at $T \sim 10^6$ K in the [2.0-5.0] and to $\leq 1\%$ in the [5.0-7.0]keV range, respectively.

In Fig.13 we compare instead the distribution of the detectable fraction of the sky model for *Athena*, eROSITA and XMM, for hypothetical 10 ks (dot-dash lines), 100 ks (dashed) or 1 Ms (solid) exposures. The better performances expected from *Athena* across the entire energy range stem for the large collecting area in each energy bin. Owing to their smaller $A_{\rm eff}$, for the same exposures XMM and eROSITA yield significantly lower (factor $\sim 2-3$) detection fraction for $\leq 10^7 K$ in the [0.3-0.8]keV and [0.8-1.2]keV bands, while their performances drop more (~ 10) in the ≥ 1.2 keV energy range. Below 1.2 keV, our statistics suggest that $\sim$ 1Ms integrations with XMM and eROSITA would be competitive with a ~ 100 ks intergation with ATHENA. However, in practice eROSITA is designed to perform shallower all-sky surveys (e.g. Borm et al., 2014), integrating for ≈ 1.6 ks in most of the sky, and up to ≈ 20 ks for the regions around the poles.

[8] We use the responses available for each telescope at the following addresses: https://www.the-athena-x-ray-observatory.eu/resources/simulation-tools.html (for *Athena*), http://www2011.mpe.mpg.de/eROSITA/response/ (eROSITA), https://www.cosmos.esa.int/web/xmm-newton/epic-response-files (XMM-Newton).

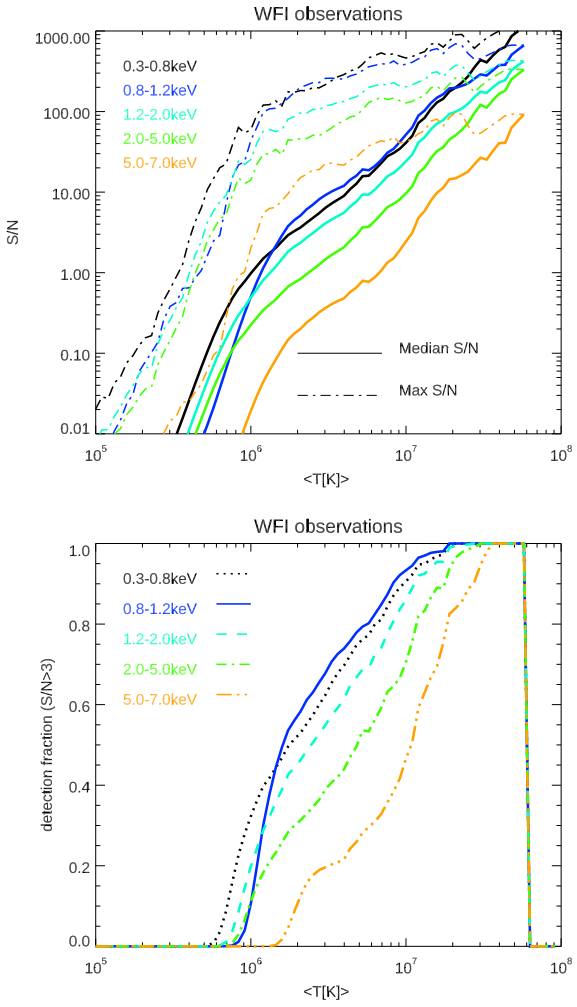

Fig. 12: Top panel: median and maximum S/N of pixels in our simulated WFI observation, assuming a 1Ms integration, as a function of environment and for different energy ranges. Bottom panel: fraction of pixels with $S/N \geq 3$ as function of temperature and energy bands for the same mock WFI observations .

Table 2: Assumed values for the radio observing parameters considered in this work: central observing frequency, beam resolution, thermal rms noise per beam and detection threshold considered in our analysis (considering a 3σ detection, also including confusion noise) .

Telescope	Frequency [MHz]	beam ["]	$\sigma_{\rm rms}$ [μJy/beam]	detection thr. [μJy/arcsec^2]
SKA-LOW	260	7.3	4.8	0.24
LOFAR-HBA	120	25	250	1.05
MWA Phase I	200	120	10,000	1.83

On the other hand, $\sim$ 50 ks exposures with XMM have been performed in the outer regions of galaxy clusters, leading for example to the detection of intracluster filaments in A2774 (e.g. Eckert et al., 2015).

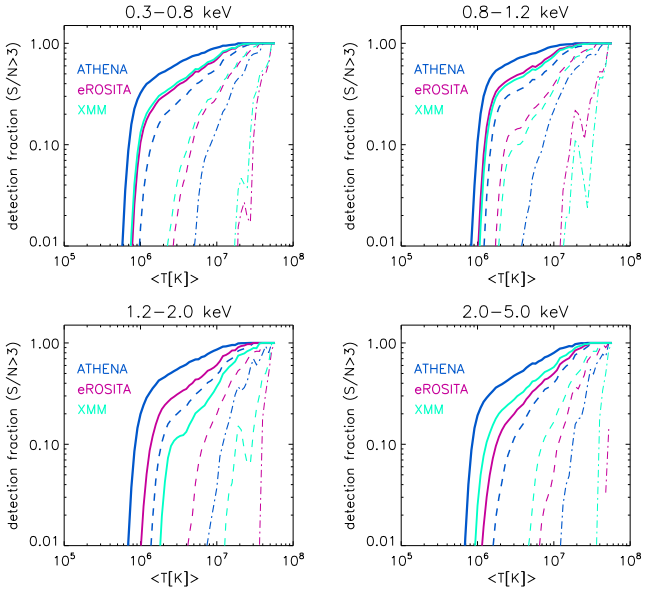

Fig. 13: Distribution of the detectable fraction ($S/N \geq 3$) of the simulated cosmic web as a function of the projected mass-weighted gas temperature, for the different X-ray satellites considered in this work, for different energy ranges and considering a 10 ks (dot-dashed lines), a 100 ks (dashed) and 1Ms (solid) integration.

3.3.2. Radio: SKA-LOW and LOFAR

We also produced mock radio observations at a given frequency ν, for the all-sky survey planned for MWA, LOFAR-HBA and SKA-LOW with a procedure similar to Vazza et al. (2015b) and Vazza et al. (2015a). The radio sky models were transformed using Fast Fourier Transform to remove the frequencies below the minimum antenna baseline of each specific radio configuration, i.e. we mimic the loss of signal from scales larger than those sampled by the minimum instrumental baseline. This is particularly relevant for the large-scale diffuse gas emission from filaments and cluster outskirts, even if all these low-frequency telescopes are suitable to well sample such large-scale fluctuations, as well as telescopes working at $\sim$ 1.4 GHz. Our maps are converted back into real space and the emission is convolved for the resolution beam with a Gaussian filter, and the detectable emission is only that $\geq 3\sigma_{\rm rms}$ (where $\sigma_{\rm rms}$ is largest between the thermal or the confusion noise of each instrument). In this simplistic approach we assume that it is possible to entirely remove galactic foregrounds (e.g. Bonaldi & Brown, 2015) and point-like radio sources (e.g. van Weeren et al., 2016), so that the theoretical thermal/confusion noise (e.g. Loi et al., 2019) of each instrument can be reached.

The details of the mock observing parameters considered in this work are given in Tab.2, in which we compared the performances of our reference SKA-LOW 260 MHz observation to the lower 120 MHz central frequency of LOFAR-HBA and to a 200 MHz observation with MWA Phase I. The left panels of Fig.10-11 show the mock radio observation of our 100^3 Mpc^3

box at $z = 0.05$ at the central observing frequency of 260 MHz, assuming the resolution, baseline sampling and sensitivity of the SKA-LOW observing conditions given in Tab. 2. The typical trends of detections we can expect from these instruments applied to the quest for the cosmic web have been already discussed at depth in previous work (e.g. Vazza et al., 2015b, 2017a) and are applicable also here, albeit for SKA-LOW we consider the most updated predictions on the survey performance.

While our main focus here is to assess the potential of each all-sky radio survey in detecting promising candidates for longer X-ray integrations outside of the virial region of clusters, the peak performance on diffuse emission that each radio telescope can achieve are slightly larger, i.e. by observing the same target for longer exposures and/or tapering the data to a coarser resolution to increase the surface brightness sensitivity, if confusion noise is not the limiting factor. We comment on this issue more diffusely in the next Section. In general, the conclusions reached in our previous works (Vazza et al., 2015a,b, 2017a) apply also here: while the SKA-LOW promises to detect with higher fidelity a non-negligible fraction of the radio emitting cosmic web, both LOFAR and MWA should be able to perform earlier detections of cluster outskirts and emission in-between interacting clusters.

3.3.3. What can be detected with realistic observations?

Simulations can help us in defining the most efficient strategy to select targets for long spectroscopic analysis of cluster bridges.

Based on our catalog of halos, we extracted all possible close cluster pairs, with the priors that their virial spheres (based on R_{100}) should not overlap, and that their *projected* separation is smaller than four times $R_{12} = R_{100,1} + R_{100,2}$. We then select a rectangle along the line connecting their centres, starting from one virial radius and ending onto the other, with a $5'$ width, which corresponds to *Athena*'s X-IFU field-of-view.

An example is shown in Fig. 14, where we show mock radio and X-ray observations of two bridges connected to a $\sim 2 \cdot 10^{14} M_{\odot}$ galaxy cluster. Contours indicate the regions that can be detected at $\geq 3\sigma$ in the different frequencies.

All radio surveys should be able to detect emission from shocked gas in the larger bridge in the center of the image, while only SKA-LOW should detect some small emission patches in the smaller bridge. While the sensitivity in surface brightness can be increased by changing the observing strategy, for example by ad-hoc tapering, e.g. Botteon et al. (2018)), the high spatial resolution of SKA-LOW ($\theta = 7.3$") is key to resolving the intricate shock network in bridges. In the same figure we also show that, unlike in the case of large-scale diffuse emission expected from cosmic filaments, the relatively small-scale ($\leq 5 - 10'$) emission from shocks in bridges is also well-sampled at higher frequencies. In this case, observations at 1.4 GHz with ASKAP or SKA-MID could detect this emission.

Moreover, the possibility of observing polarised emission from such regions will enable SKA-MID to make more significant detections since polarisation reduces the dynamic range and the confusion level, which is the biggest constraint for SKA-LOW (e.g. Vazza et al., 2015a).

The lower row shows the performance of X-ray observations, considering a 1 Ms *Athena*-WFI integration of the same region, 100 ks with XMM or 1.6 ks as in the eROSITA all-sky survey. Clearly, the detections of such regions in X-rays will remain a challenge, in which only *Athena* promises some joint detection with radio observations.

In order to quantify the performances of real observations of intracluster bridges, we extracted from our catalog of pairs the fraction of the connecting rectangle ($5'$ wide) that can be significantly detected with various instruments and observing techniques. We then averaged the results by rescaling by the distance between the two virial spheres. With a few variations in the selection criteria and in the observing techniques, we find:

- *performance of X-ray vs radio observations:* in Fig. 15 we show the mean detectable fraction of intracluster bridges as a function of the distance from one virial radius to the other, and normalized for the projected separation between the two virial radii. We extracted here all pairs of clusters with $M_{100} \geq 8 \cdot 10^{13} M_{\odot}$ and found at a $\leq 4R_{12}$ distance, both in projection and in 3D (50 pairs in total). We consider here *Athena*-WFI 1Ms and 100 ks integrations, XMM 100 ks integration and eROSITA 20 ks integration, and observations with SKA-LOW, MWA Phase I and LOFAR-HBA surveys. On average, XMM and eROSITA integrations give a very little detection fraction (we also performed the analysis of a 1.6 ks survey with eROSITA, which yields virtually null detections in the entire sample, see e.g. the lower right panel of Fig.14). *Athena*'s 1Ms integration may instead detect a $\sim 10 - 15\%$ of the surface of intracluster bridges, but also a 100 ks integration with the same telescope will detect a significant $\sim 5 - 9\%$ of it. As expected, the situation is clearly better in the radio domain as an SKA-LOW survey should be able to detect $\sim 20\%$ of the intracluster filaments area, and MWA Phase I and LOFAR-HBA surveys at least of $\sim 10 - 15\%$ of it. We remark that for radio surveys the detectable (area) fraction is not an unambiguous proxy for the real performance of each telescope, because the rectangle we consider here has a thickness ($5'$) close to the beam size of MWA Phase I observations ($2'$) or of what is typically achieved for tapered LOFAR-HBA observations (50"). Hence, a few detected beams can contribute to a large covering fraction, yet at the cost of a loss in spatial detail, which is crucial (see Fig.14) if the emission is produced by several shock waves. SKA-LOW will reach the maximum depth after only ≈ 10 hours of integration (due to the confusion limit), but it should be able to give a detailed spatial information on shocks within the bridge regions, which can also allow a detailed modelling of particle spectra and ageing.
- *separation between cluster pairs:* in Fig. 16 we show that if the only prior is on the projected separation (grey lines)

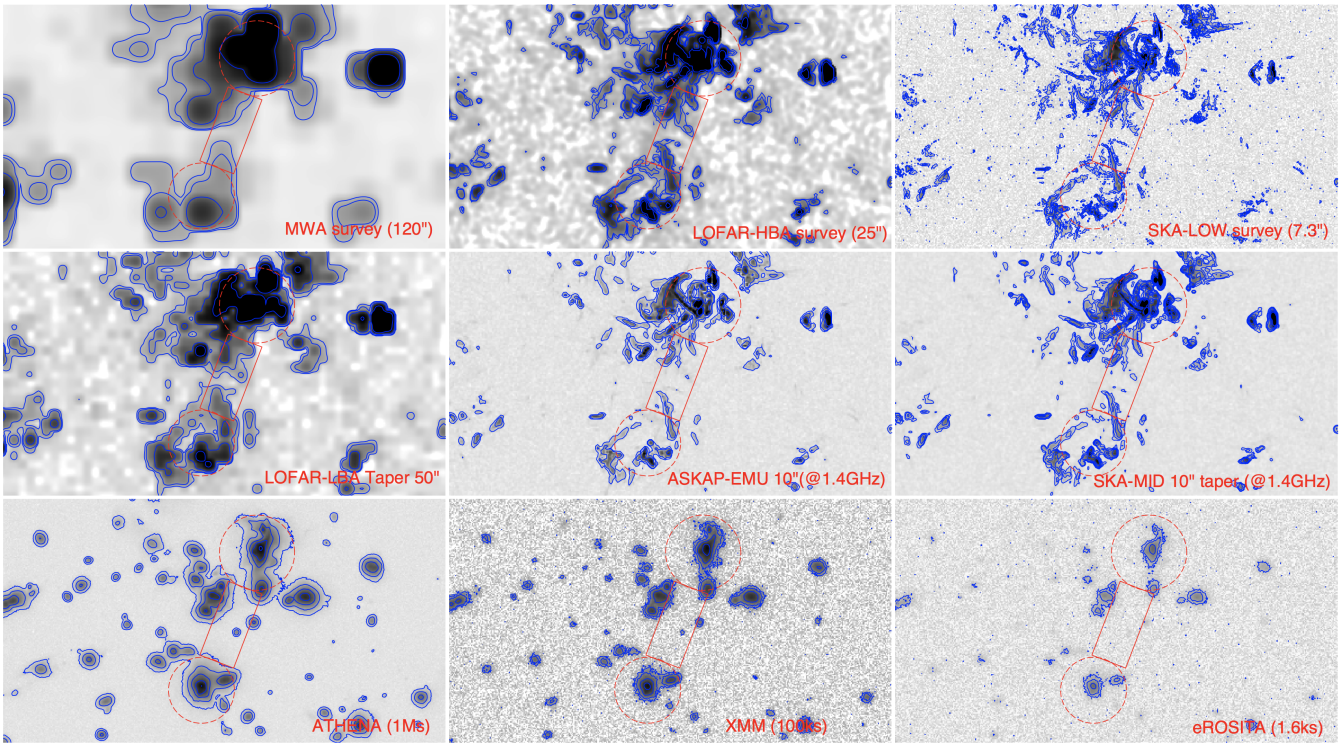

Fig. 14: Example of mock radio (top two rows) and X-ray (bottom row) observations of two bridges connected to a $\sim 2 \cdot 10^{14} M_{\odot}$ galaxy cluster in our simulation. The red circles denote the R_{100} of the halos connected by bridges with width $5'$ (red rectangles), as in Sec. 3.3.3. In all panels, we give in colors the signal and noise of each mock observation, convolved for the resolution of each observation, while the blue contours are drawn with a logarithmic spacing, starting from 3 S/N of each observation (see text for explanations).

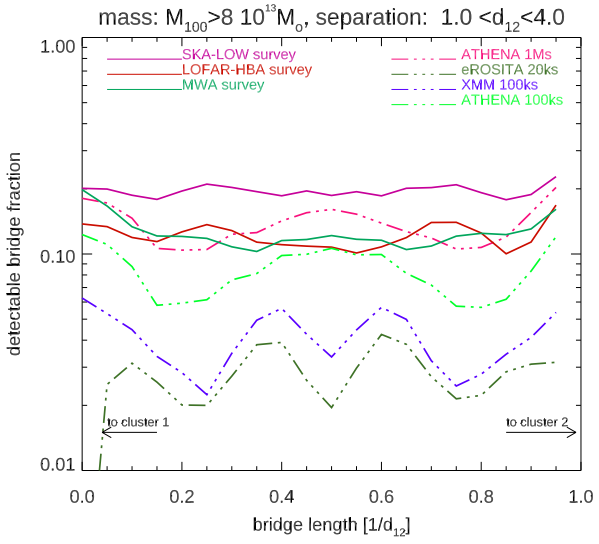

Fig. 15: 1-dimensional profile of the detectable bridge fraction connecting pairs of clusters with mass $M_{100} \geq 5 \cdot 10^{13} M_{\odot}$, considering different X-ray (solid lines) or radio (dot-dashed) observing configurations.

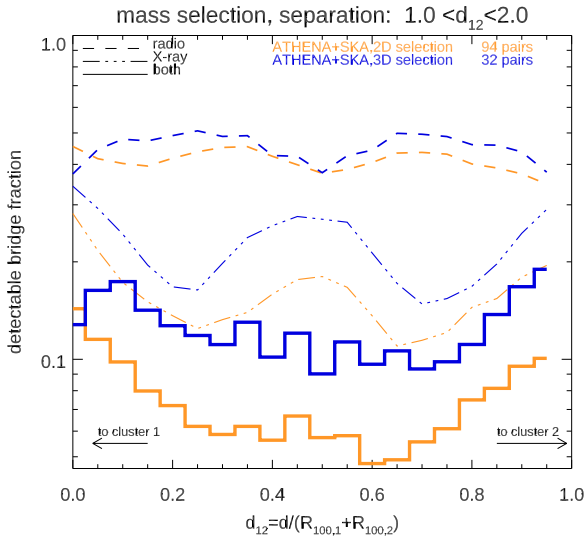

Fig. 16: Detectable fraction of bridges connecting pairs of clusters with mass $M_{100} \geq 10^{13} M_{\odot}$ and for *Athena* and SKA-LOW observations, for samples of cluster pairs selected only based on their projected (2D) separation, or including also a limit to their physical (3D) separation.

a good fraction of the bridge is detectable with a 1 Ms integration with *Athena*. However, only $\sim 10 - 20\%$ is detectable with SKA-LOW, up to a distance of twice d_{12}.

If we only consider clusters that are *physically* related, by imposing an additional prior ($d_{3D} \leq 10\ d_{12}$) on their

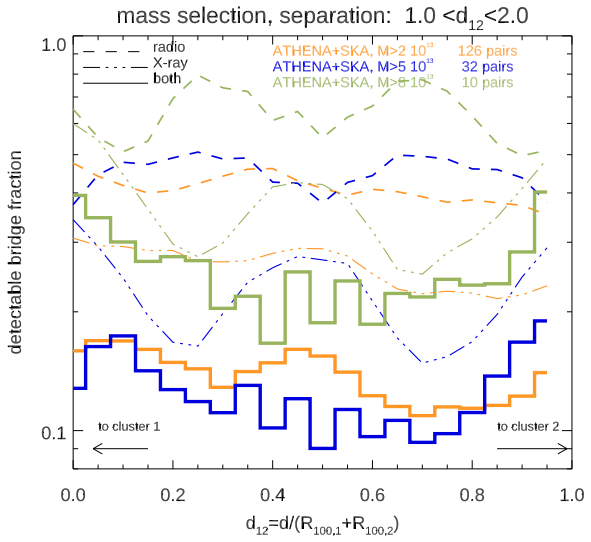

Fig. 17: Detectable fraction of bridges connecting pairs of clusters with mass $M_{100} \geq 10^{13} M_{\odot}$ and for *Athena* and SKA-LOW observations, for samples of interacting clusters chosen after imposing an increasing lower bound for the minimum mass.

3D distance, the chances of detections in radio, and hence of joint detections, increase very significantly and reach $\sim 15-20\%$ close to clusters. This follows from the fact that indeed the detectable radio emission is mostly produced by shocks associated with *physical* gas perturbations triggered during the early merger stage of such objects, rather than to the simple superposition of the shocked outer layers of galaxy clusters which are not interacting;

– *effect of mass selection:* in Fig. 17 we show the effect of using a higher mass threshold for the selection of our couples of objects (always connected also in 3D, using the previous prior). The fraction of the joint detection steadily increases by using higher masses, even though the total number of objects goes down. For the highest mass selection, $\sim 20\%$ of the central bridge area (and $\sim 30\%$ closer to clusters) can be detected, both, by *Athena* and SKA-LOW.

The limited volume of our simulation does not allow us to test a large number of cluster pairs, hence our work can only identify global trends across the investigated cluster population. We conclude that the best strategy to detect X-ray emission from the WHIM in intracluster bridges is to select cluster pairs with short physical and projected separation ($1 \leq d/R_{12} \leq 4$, where $R_{12} = R_{100,1} + R_{100,2}$, with large masses ($M_{100} \geq 10^{14} M_{\odot}$) and with the additional prior of having detected radio emission between them. In this case, our simulations suggest that investing ~ 1 Ms of integration with *Athena* should also result into a detection of the WHIM in emission from $\sim 20-30\%$ of the connecting area, which can in principle be suitable for spectroscopic analysis with X-IFU.

3.3.4. A pilot X-IFU observation of a gas bridge between interacting clusters

Finally, we conducted a pilot study of a potentially promising target for future 1 Ms *Athena* X-IFU observations, applying the end-to-end X-IFU pipeline outlined in Roncarelli et al. (2018).

We performed the ENZO AMR re-simulation of a galaxy cluster in an early merger state at $z = 0.1$, with a total mass of $M_{100} = 6.37 \cdot 10^{14} M_{\odot}$ and a virial radius of $R_{100} = 2.05$ Mpc.

We selected this cluster from a different parent simulation, using nested initial conditions and 7 additional levels of AMR to increase the maximum spatial resolution to $\Delta x_{\rm max} = 3.95$ kpc, as in Vazza et al. (2018b). This cluster has been specifically selected as it shows at $z = 0.1$ an ongoing merger with a second massive galaxy clusters (e.g. Dominguez-Fernandez et al. submitted), with indication of strong dynamical activity in the $R_{100} - R_{200}$ radial range from the first cluster. Moreover, by applying the same mock observation techniques introduced in the previous Sections, we identified in this object a patch, located in-between the two clusters, in which a significant detection will be possible both with SKA-LOW and with a long *Athena*'s integration. We also analysed this object using the multi-scale filtering technique to detect shocks and turbulent motions (and further decompose their velocity field into compressive and solenoidal components) as in Vazza et al. (2017b).

As shown in Fig. 18, the region in between the two colliding clusters is $T \sim 5-6$ keV, significantly hotter than the surrounding ICM, as an effect of the ongoing merger. Not shocks but rather compression is responsible for this level of heating, as the outer cluster shells of the interacting clusters get compressed at the velocity of $\sim 500 - 700$ km/s and the average density in the bridge is $\sim 10^2 \langle \rho_b \rangle$ (where $\langle \rho_b \rangle$ is the cosmic mean baryon density). Due to the large temperature and sound speed here, no strong accretion shocks are found, but we rather measure a network of $\mathcal{M} \sim 2-5$ shocks, intermittently driven by the event. Our turbulent filtering detects turbulent velocity of order $\sim 400 - 500$ km/s in this region, almost equally divided into solenoidal and compressive components, with a typical outer scale of ~ 400 kpc. The magnetic field in the bridge region where radio and X-ray emission can be detected is $B \sim 0.1 - 0.2$ μG, which yields a plasma beta parameter of order $\beta_{\rm pl} = n k_b T / (B^2/8\pi) \sim 5000$.

We extracted from this region a $(75 \times 75 \times 4800)$ kpc^3 volume that contains entirely the emitting regions, as well as the outer regions of the two clusters in the field of view. The region's z-axis is aligned with the line-of-sight. Following Roncarelli et al. (2018), we simulated with 1 eV resolution the X-ray emission assuming an APEC model (version 2.0.2, Smith et al., 2001), absorbed with a Galactic equivalent hydrogen column density $n_{\rm H} = 2 \times 10^{20}$ atoms cm^{-2}. We assume a rather conservative value of (spatially constant) metal abundance $Z = 0.2\ Z_{\odot}$ with respect to the solar abundance in Anders & Grevesse (1989). To provide a realistic observational setup, we included a X-ray background modelled by (i) two thermal local components with temperatures of 0.099 and 0.225 keV and normalization for the adopted APEC model of 1.535 $\times 10^{-6}$ per arcmin^2 of integrated area, respectively,

both with solar metallicity and only the second one absorbed by $n_{\rm H}$ and with a normalization reduced by a factor of 0.42 (see McCammon et al., 2002) and (ii) a cosmic X-ray background, assumed unresolved at the 20% level, simulated with an absorbed power-law with a photon index of 1.5 and normalization of 2.1×10^{-7} photons/keV/cm^2/s/arcmin^2 at 1 keV (see also, e.g. Lotti et al., 2014). After projecting these spectra into the sky plane, we used the resulting signal as an input of the SIXTE simulator [9] (Schmid et al., 2013), assuming 1 Ms exposure. An updated instrumental particle background (Lotti et al., 2017) is already implemented in SIXTE. The output of the SIXTE code consists of a realistic mock X-IFU observation, i.e. an observed event-list containing a total of $\sim$ 16500 counts[10] (0.3–10 keV) from a 0.382 arcmin^2 area in the center of the X-IFU field. These photons were folded in single spectrum that has been jointly fitted with a spectrum containing only the expected photons from a background modelled as described above, using a Cash statistic (Cash, 1979) implemented in XSPEC (Arnaud, 1996). To derive the thermodynamic and kinematic properties of the gaseous component associated to the cluster, we assumed a BAPEC model with 5 free parameters, namely normalization, temperature, metal abundance, redshift and velocity dispersion ($n_{\rm H}$ has been fixed to the input value) and proceeded with a blind fitting analysis.

In Fig. 20, we show the mock spectra and the fit results, with the three components (thermal, X-ray and particle background). The results of the X-IFU spectral fitting simulation are also shown in table 3, together with the reference values, computed as the averages on the simulation cells. Thanks to the 1 Msec exposure, temperature (compared to the spectroscopic-like) and metallicity are recovered with high precision with a typical statistical error of 0.3–0.4 keV and 0.05 $Z_\odot$, respectively. Most importantly, the evidence of a significant velocity dispersion is detected at high significance (more than 2.5σ), albeit with a relatively high statistical error. All the quantities are recovered with no apparent systematic bias.

However, we notice that our setup assumes a perfectly known (X-ray and particle) background. To relax this unrealistic assumption, we have also run 100 Monte-Carlo spectral simulations assuming the cluster component and propagating random fluctuations, consistent with the current expectations on the background reproducibility in X-ray, on $n_{\rm H}$ (at 1% level), on the particle background (2%) and on the remaining parameters of the background model, i.e. the thermal components and the power-law for the unresolved cosmic X-ray background (5%). We estimate the following systematic scatter in the distribution on the best-fitting measurements of the 5 parameters of the BAPEC model: $\sim$ 2%, 6%, 27%, 58% and $<$1% on normalization, temperature, metal abundance, line broadening and redshift, respectively. These results show that, while most of the parameters will be only limited by the photon counts statistic, the characterization of the emission lines in terms of total metallicity and broadening at this level of surface brightness will depend on a reliable modelization of the underlying background.

Table 3: Physical properties of the plasma computed in the simulation volume compared to the ones measured through the end-to-end X-IFU simulation, with spectral fitting, for a 1Ms integration. The reference (input) temperature is the spectroscopic-like, v and w are the emission weighted averages and A is the metal abundance, computed in the simulation volume as in Roncarelli et al. (2018).

Field	Input (sim)	Output (X-IFU)
T [keV]	5.52	5.33 $\pm$ [-0.31, 0.40]
v	65	215 $\pm$ [-146, 123]
w	465	384 $\pm$ [-148, 144]
A [1/$Z_\odot$]	0.20	0.25 $\pm$ [-0.05, 0.06]

These first results offer an interesting physical application to the study of shock waves and particle acceleration in the periphery of galaxy clusters: namely a new method to constrain the shock Mach number based on spectroscopic analysis. If we assume that the measured velocity dispersion is similar to the velocity jump induced by the shock, $w \approx \Delta v' = \Delta v / \cos\phi$ (in which ϕ is the inclination of the shock normal with respect to the line of sight), and that the local sound speed is given by the temperature probed by the spectroscopy, through the "velocity-jump" method (Vazza et al., 2009) we derive

$$\mathcal{M}_{\rm XIFU} = \frac{2}{3}\left(\frac{\Delta v'}{c_s} + \sqrt{\frac{4\Delta v'}{c_s} + 9}\right) \quad (2)$$

which yields $\mathcal{M}_{\rm XIFU} \approx 2.42$ for the X-IFU best fit values of $T \approx 5.33$ keV, $w \approx 465$ km/s and considering $\phi \approx 75^\circ$ for the shock normal (as suggested by Fig. 19, right panel). This is is not too off from the $\mathcal{M} \sim 2.5 - 3$ range of Mach number we can measure in 3D within the X-IFU's Field of View, and suggests the interesting possibility of an independent way of constraining the shock parameters via spectroscopic analysis, to be combined and compared with the available radio information there (e.g. Mach number estimated from radio spectral indices for high resolution observations and particle acceleration efficiency). We comment that intracluster bridges, given their particular geometrical selection, may allow performing this study in a more robust way than in more internal regions of galaxy clusters, where radio relics are found, because in these external regions the local sound speed is low enough, and the velocity field is large enough, that the Doppler broadening due to shocks with a large inclination along the line of sight may be clearly detected via spectroscopic analysis.

4. Discussion: Physical and Numerical uncertainties

Our results are based on non-radiative MHD simulations, in which the role of galaxy formation processes are neglected. This introduces a number of caveats in our analysis, connected

[9] https://www.sternwarte.uni-erlangen.de/research/sixte/

[10] As a further reference to the reader, we verified that $\sim$8900 counts are coming from the source (i.e. the simulated plasma), while $\sim$ 5400 and $\sim$ 2200 from the X-ray and particle background, respectively. This piece of information, that would not be available to the observer, has been omitted in the following analysis.

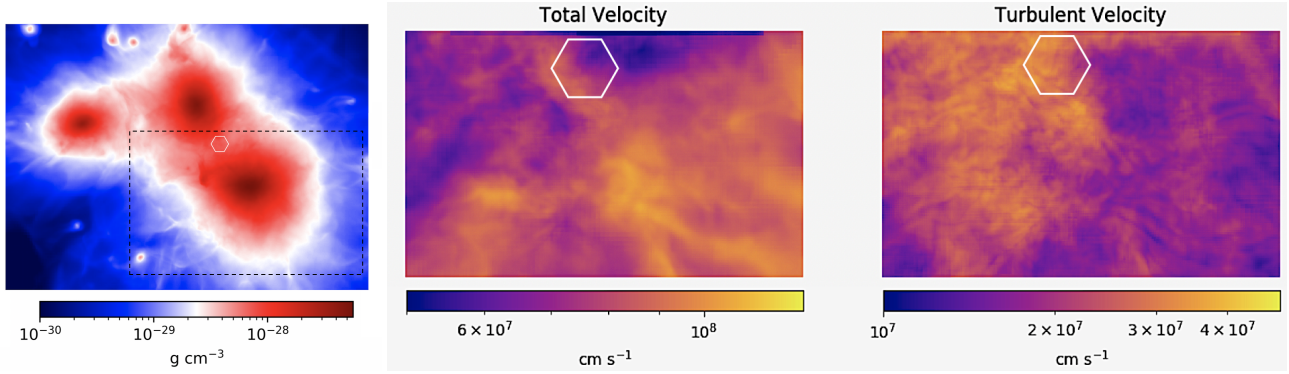

Fig. 18: Left panel: projected mean gas density for the interacting cluster used for our SIXTE simulation in Sec.3.3.4. Central and Right panels: projected (volume weighted) map of total gas velocity module and of turbulent velocity module for a zoomed region in the left panel. The additional white region shows the $5' \times 5'$ region used for our SIXTE mock observation.

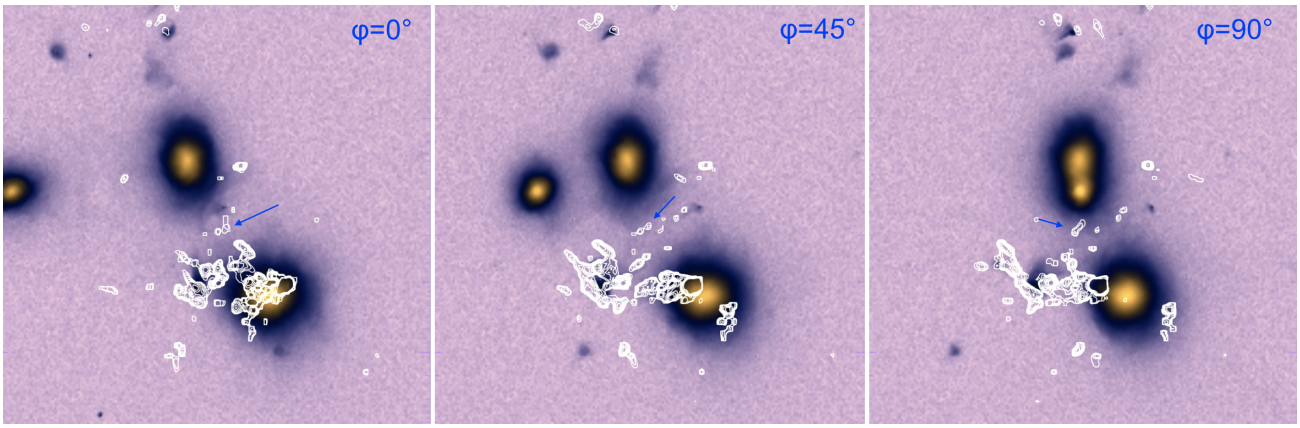

Fig. 19: Three different rotations ($0°$, $45°$ and $90°$) around cluster E5A, showing the X-ray counts (colors) and the detectable radio emission at 260 MHz (contours). The additional blue arrow give the approximate location of the detectable emission region in the rotated images.

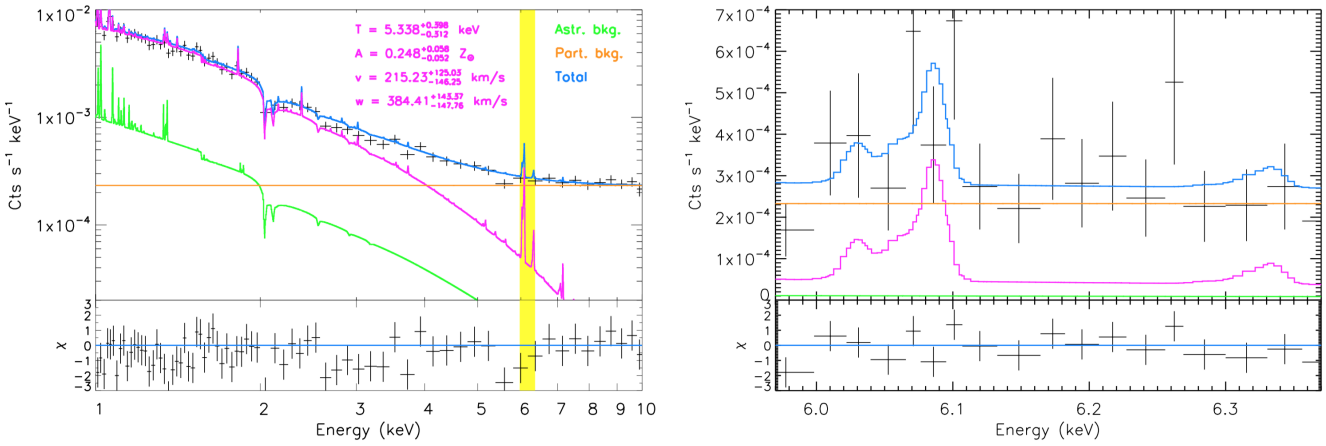

Fig. 20: Left panel: X-IFU simulated spectrum of the gas bridge and its spectral analysis. Spectral data points with error bars (black crosses) are shown with the best-fit model (blue solid line) and its three components: thermal emission from the gas (magenta), X-ray astrophysical background (green) and particle background (orange). Fit results, with errors, for the four physical quantities of the gas components are also shown. The bottom subpanel shows the residuals with respect to the model. Right panel: same as left panel, but zooming on the 6–6.4 keV energy range (highlighted in yellow in the left panel) where the most prominent emission lines (blended Fe XXV and Fe XXVI K complexes) are present. In both panels data points have been rebinned for display purposes. The plot scaling for the spectra is logarithmic and linear in the left and right panels, respectively.

with the lack of energy losses (e.g. radiative cooling processes) and feedback processes.

In general, we expect the most relevant effects of cooling and feedback to be limited to cluster centres. While for $\leq 0.2\ R_{100}$ the combined effect of cooling, star formation and feedback (stellar or AGN ones) can introduce a significant amount of clumping in clusters (Roncarelli et al., 2006a; Nagai & Lau, 2011), as well as increase the gas density in cluster cores $\sim\ 10$ times compared to non-radiative simulations. However, such effects are predicted to be negligible at distances larger than $\sim R_{100}$ (e.g. Vazza et al., 2013), as well as within intracluster bridges.

The absence of galaxy formation processes limits our ability to model the 3D distribution of metals in the outer regions of galaxy clusters. Hence, we assume a uniform $Z = 0.3 Z_{\odot}$ gas metallicity. The assumption of uniform metallicity for all elements reduces the number of free parameters making the spectral fitting presented in Section 3.3.4 easier. In reality, as pointed out by Cucchetti et al. (2018), the X-IFU spectral analysis will require a detailed treatment of the various emitting ions due to the chemical complexity of the ICM (see also Roncarelli et al., 2010; Biffi et al., 2013). However, we stress that most of the information on w is encoded in the Fe XXV and Fe XXVI K complexes lines (see the right panel of Fig. 20), so this simplification has a minor impact on the accuracy of our results. Fig. 21 shows the X-ray emissivity in in three X-ray bands [0.3-0.8] keV, [0.8-1.2] keV and [2.0-10.0] keV, as a function of temperatures and for increasing gas metallicity. While the realistic chances of detecting filaments in X-ray should vary as a function of metal abundance there, in the $\geq 10^7$ K temperature range of intracluster bridges the impact of metal line emission is overall negligible and is not critical for detections with *Athena*-WFI.

More critical is the level of gas metallicty for any spectrosopic attempt of characterizing the local plasma condition, as in our mock X-IFU observation of Sec. 3.3.4. However, in this case we used already the more conservative value of $0.2\ Z_{\odot}$ (spatially uniform everywhere) for our 1Ms mock XIFU observation, and showed that also in this case a robust measurement of local plasma parameters is possible, provided that the particle and instrumental background are under control. Our tests also indicate that conversely if $Z \geq 0.1 Z_{\odot}$ in intracluster bridges, the reconstruction process of gas conditions through spectroscopic analysis (even with a 1Ms integration) will unreliable and dominated by too large uncertainties. However, the state of the art observational and theoretical description of the outer regions of galaxy clusters suggests that a $\sim 0.1 Z_{\odot}$ metallicity is probably even too conservative, and that larger metallicity values should be there (e.g. Biffi et al., 2018; Mernier et al., 2018).

It shall be noticed that, recently, Khabibullin & Churazov (2019) reconsidered the contribution from the resonantly scattered cosmic X-ray background in to the line emission for the warm-hot intergalactic medium. This implies a boost up of the intrinsic emissivity of the WHIM, considered in this work, by a factor $\sim\ 30$ from resonantly scattered lines. However, this boost is limited to the gas at $T \leq 10^6$ K and, when integrated in the [0.5-1] keV band, it is of order of $\sim\ 4$ for the coldest part of the WHIM only. Therefore, this effect is not expected to contribute to the detectability of the much hotter gas located in intracluster bridges, leaving all our main conclusions unaffected.

Finally, our mock radio emission depends on the assumed model for extragalactic magnetic fields, as well as on the assumed electron acceleration efficiency by shocks. Overall, it is plausible that both factors contribute to make our previous estimates a *lower limit*. For the electron acceleration, we shall notice that our acceleration model only includes *direct* acceleration of electrons from the thermal pool (Hoeft & Brüggen, 2007), but it neglects the effect of shock re-accelerated electrons, which may be non-negligible in the Mach number range of shocks in bridges (Pinzke et al., 2013; Kang et al., 2012). The level of fossil electrons in cluster outskirts and in bridges is however highly uncertain, but in any residual level of fossil electrons will contribute to increase the emission beyond our estimates, even if the emission by $\mathcal{M} \geq 3 - 4$ shocks is expected to be always dominated by the injection of "fresh" electrons (Pinzke et al., 2013).

Also, in our model we neglected for simplicity any further injection or re-acceleration of electrons by additional processes (e.g. turbulent reacceleration, re-connection, shock drift acceleration etc. e.g. Brunetti & Jones 2014 and Bykov et al. 2019 for recent reviews) which may power the emission, expecially at low frequency, beyond our estimates.

Recent LOFAR-HBA observations suggest indeed that more volume filling and diffuse radio emission processes may be present on $\sim \mathrm{Mpc}$ scales outside of galaxy clusters (Govoni et al., submitted).

Magnetic fields may in principle be overstimated in cosmic filaments, in case the seed field are not of primordial origin and/or there is no dynamo amplification capable to increase the magnetisation of the WHIM to the $\sim 10\ \mathrm{nG}$ level (Vazza et al., 2017a). Conversely, limited to the environment of intracluster bridges, our AMR simulation can resolve ongoing dynamo amplification of seed fields, albeit with final fields strengths which are typically far from equipartition with the kinetic energy, at least in our simulation (e.g. Locatelli et al., 2018). The contribution from un-resolved gas motions by the finite numerical resolution in our scheme may underestimate the level of small-scale dynamo amplification, which gets independent from the ampitude of seed fields for large enough Reynolds number (e.g. Cho, 2014; Beresnyak & Miniati, 2016). If this is the case, the $\sim\ 0.1 - 0.2\ \mu\mathrm{G}$ we measured for our intracluster bridge in Sec.3.3.4 may be underestimated, even if to our knowledge this run is the most resolved so far for objects of this kind.

5. Conclusions

We have presented mock radio and X-ray observations of the comic web, based on recent cosmological simulations obtained with the cosmological MHD code ENZO (Bryan et al., 2014). Extending our first exploratory study in Cassano et al. (2018), we quantified the chances of "double detecting" the shocked

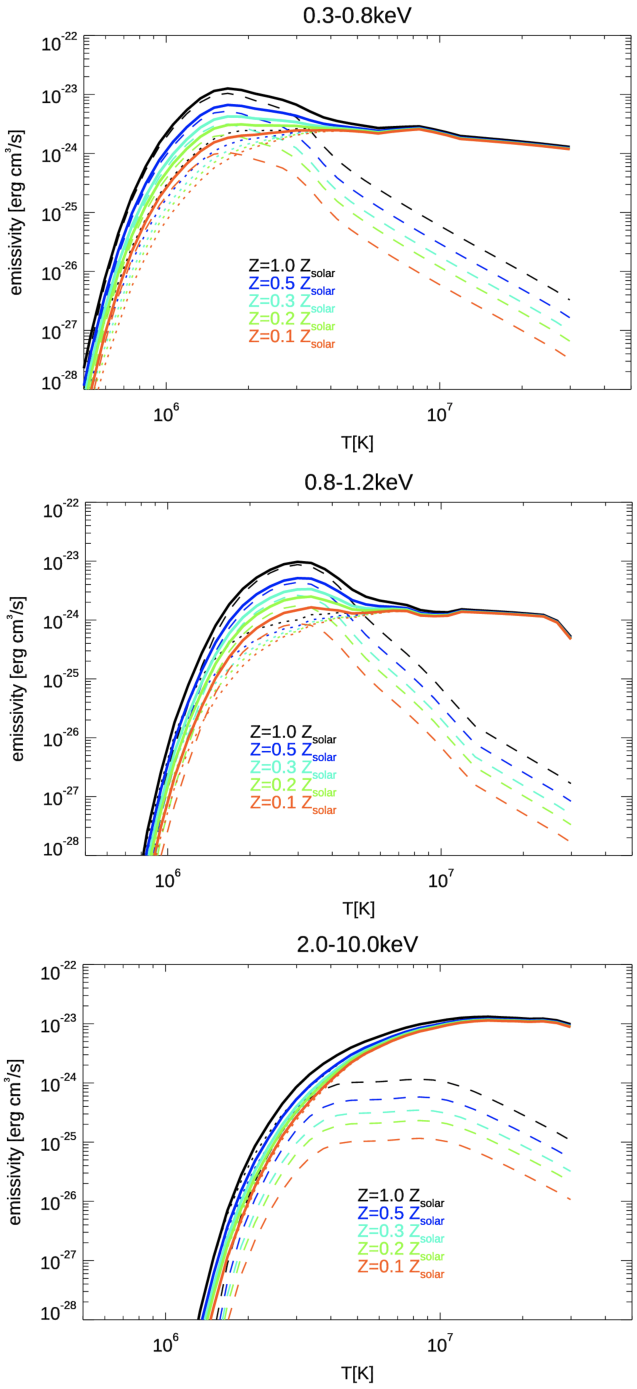

Fig. 21: X-ray emissivity as a function of temperature for gas of different metallicities, simulated with an APEC emission model.

cosmic web in both frequency ranges, and propose best observing strategies tailored for future instruments (e.g. SKA and *Athena*). Our study highlights that the most promising targets for double detections outside of galaxy clusters are typically located in matter "bridges" connecting pairs of galaxy clusters in an earlier merger state. At this interaction stage, both radio and X-ray emission are boosted compared to the more typical conditions found in cluster outskirts. Such (transient) excess emissions appear to be within the detection range of existing (LOFAR, MWA, ASKAP) and future (SKA-LOW and SKA-MID) radio surveys, as well as of very long (≥ 100 ks) integrations with *Athena*, XMM and eROSITA. Based on our simulations, the chances of double detections get greatly increased for pairs of objects with a physical (3D) association, with masses in excess of $\geq 10^{14}$ M$_\odot$ and with a projected separation between 1 and 4 mean virial diameters (e.g. the sum of the two virial radii of interacting clusters). For practical purposes, a prior detection of such bridges in the radio domain is expected to serve a strong indication of the possibility of detecting emission also in the soft ($\leq 1.2-2$ keV) X-ray band.

Detecting radio emission from transient shocks in such systems will also represent a strong motivation to attempt long dedicated integrations with *Athena*'s X-IFU. For example, a deep ($\sim$ 1 Ms) integration with X-IFU on such jointly detectable portion of intracluster bridges should represent a new strong scientific case to study plasma shock physics in the rarefied environment of the WHIM, namely by allowing the derivation of the shock Mach number, entirely from spectroscopically-derived information of the local gas velocity dispersion and of the local sound speed, in a temperature regime which is difficult to find in galaxy clusters (Sec. 3.3.4).

We remark that closely interacting pairs of galaxy clusters have already been detected, and observations have highlighted unexpected thermal and non-thermal gas features in the interaction region of galaxy clusters in an early merging state (e.g. Akamatsu et al., 2017; Sugawara et al., 2017; Caglar & Hudaverdi, 2017; Botteon et al., 2018; Bonafede et al., 2018; Alvarez et al., 2018). Also Sunayaev-Zeldovich observations of close pairs have hinted the presence of dense and X-ray undetectable gas in such associations (Planck Collaboration et al., 2013; Bonjean et al., 2018).

Such objects are clearly different from "standard" cosmic filaments that are produced by simulations on much larger scales (e.g. Gheller et al., 2016). Moreover, the gas in these bridges is on a thermodynamical state which is different from the standard WHIM, as the typical density and temperature values are a factor ~ 10 larger than in the WHIM, and more into the ICM ballpark. However, simulations suggest that bridges are relatively short-lived ($\leq$ Gyr), and should undergo a fast evolution compared to filaments on a larger scale, and used to be part of the standard WHIM a $\sim$ Gyr ago, before becoming observable in the X-ray band. For this reason they have the potential of illuminating an important intermediate stage in the evolution of cosmic baryons, where gas that has been only shock-heated once in the past gets fast advected onto larger clusters and is subject to large-scale mixing, reprocessing by weaker shocks and supersonic turbulence. This leads to a transient "boosted WHIM" phase, with a mean temperature beyond the canonical (but not entirely physically motivated) temperature bounds associated to the WHIM ($10^5 \mathrm{K} \leq \mathrm{T} \leq 10^7 \mathrm{K}$).

In summary, our work can stress the importance of the radio band to study the missing baryons of the cosmic web. We quantify this by presenting in Fig.22 the distribution of the

mean temperature and gas over density for all pixels in our sky model [11]. With different contours we mark here where the 90%, 9% and 1% of the total baryon budget is at $z = 0.05$. Over-imposed to this, we color code which fraction of this budget should be detectable by X-ray observations using a 1Ms exposure with *Athena*, or with the SKA-LOW survey at 260 MHz.

Clearly, X-ray observations are maximally efficient of detecting most of baryons in the high-temperature and high-density part of the plot. However, less than 10% of the total budget of baryons in the Universe are located in this range. Conversely, radio surveys can trace only a much a smaller fraction of hot and dense baryons in the Universe, due to small filling factor of shocks leading to radio emission in this regime. However, radio detections trace baryons with significantly lower projected temperature and density compared to X-ray observations, enabling them to probe into the gas phase where $\sim 90\%$ of cosmic baryons are. As such detections can only illuminates the *shocked* portion of the WHIM (or immediately downstream of it), it will be crucial to assess the bias factor between the radio emitting fraction of the cosmic web, and its larger ("radio quiet") component. With the assistance of advanced numerical simulations, capable of assessing this bias a sa function of environment, wide and deep radio surveys will in principle have the potential to convert systematic detections of radio shocks in the rarefied cosmic web into an estimate of the total budget of "missing" baryons in Universe.

Acknowledgements. The cosmological simulations were performed with the ENZO code (http://enzo-project.org), which is the product of a collaborative effort of scientists at many universities and national laboratories. We gratefully acknowledge the ENZO development group for providing extremely helpful and well-maintained on-line documentation and tutorials. F.V. acknowledges financial support from the ERC Starting Grant "MAGCOW", no. 714196. We acknowledge the usage of computational resources on the Piz Daint supercomputer at CSCS-ETHZ (Lugano, Switzerland) under projects s701 and s805 and at the Jülich Supercomputing Centre (JFZ) under project HHH42. We also acknowledge the usage of online storage tools kindly provided by the Inaf Astronomica Archive (IA2) initiave (http://www.ia2.inaf.it). S. E. and M. R. acknowledge funding from the European Union's Horizon 2020 Programme under the AHEAD project (grant agreement n. 654215). S.E. acknowledges financial contribution from the contracts NARO15 ASI-INAF I/037/12/0, ASI 2015-046-R.0, and ASI-INAF n.2017-14-H.0. We acknowledge fruitful scientific discussions with A. Bonafede, M. Cappi, R. Cassano, G. Brunetti, I. Prandoni, E. Churazov and I. Khabibullin, which improved the presentation of our results. We also thank T. Boller and V. Ghirardini to have provided useful information on the performance of eROSITA and XMM-Newton, respectively.

References

Ade P. A. R., et al., 2015

[11] As noted in 3.1, we remark again that the mass-weighted temperature and volume-weighted gas density here *underestimate* the corresponding 3-dimensional values (where most of the emission along the LOS is produced) by ~ 10.

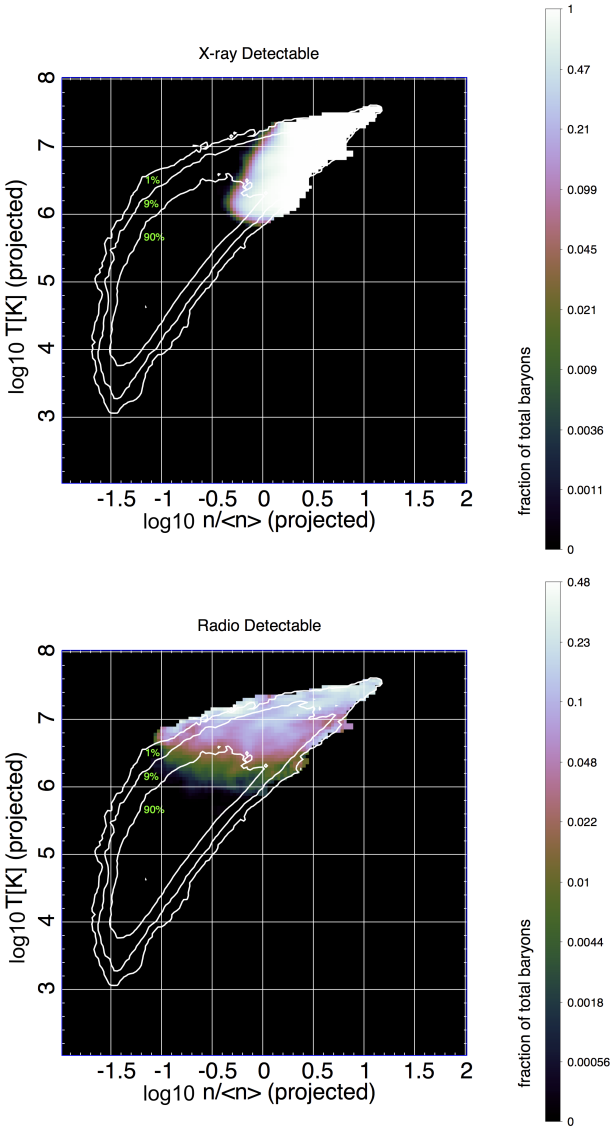

Fig. 22: Distribution of projected mean temperature and density for all pixels in our sky model at $z = 0.05$, with contours marking where the 90%, 9% and 1% of the baryon budget is. The colors marks the fraction of the total baryon budget which can be detected with X-ray detections with *Athena* (top panel) or with radio detections with SKA-LOW (bottom panel).

Akamatsu H. et al., 2017, A&A, 606, A1
Alvarez G. E., Randall S. W., Bourdin H., Jones C., Holley-Bockelmann K., 2018, ApJ, 858, 44
Anders E., Grevesse N., 1989, Geochim. Cosmochim. Acta, 53, 197
Arnaud K. A., 1996, in Astronomical Society of the Pacific Conference Series, Vol. 101, Astronomical Data Analysis Software and Systems V, Jacoby G. H., Barnes J., eds., p. 17
Bagchi J., Enßlin T. A., Miniati F., Stalin C. S., Singh M., Raychaudhury S., Humeshkar N. B., 2002, New A, 7, 249
Barcons X. et al., 2012, ArXiv e-prints
Bartels R., Zandanel F., Ando S., 2015, A&A, 582, A20
Beresnyak A., Miniati F., 2016, ApJ, 817, 127

Biffi V., Dolag K., Böhringer H., 2013, MNRAS, 428, 1395
Biffi V., Mernier F., Medvedev P., 2018, Space Sci. Rev., 214, 123
Bonafede A. et al., 2018, MNRAS, 478, 2927
Bonafede A., Vazza F., Brüggen M., Murgia M., Govoni F., Feretti L., Giovannini G., Ogrean G., 2013, MNRAS, 433, 3208
Bonaldi A., Brown M. L., 2015, MNRAS, 447, 1973
Bonjean V., Aghanim N., Salomé P., Douspis M., Beelen A., 2018, A&A, 609, A49
Borm K., Reiprich T. H., Mohammed I., Lovisari L., 2014, A&A, 567, A65
Botteon A. et al., 2018, MNRAS, 478, 885
Brown S. D., 2011, Journal of Astrophysics and Astronomy, 32, 577
Brunetti G., Jones T. W., 2014, International Journal of Modern Physics D, 23, 1430007
Bryan G. L. et al., 2014, ApJS, 211, 19
Bykov A. M., Vazza F., Kropotina J. A., Levenfish K. P., Paerels F. B. S., 2019, Space Sci. Rev., 215, 14
Caglar T., Hudaverdi M., 2017, MNRAS, 472, 2633
Cappelluti N. et al., 2012, MNRAS, 427, 651
Cash W., 1979, ApJ, 228, 939
Cassano R., Ettori S., Giacintucci S., Brunetti G., Markevitch M., Venturi T., Gitti M., 2010, ApJ, 721, L82
Cassano R. et al., 2018, ArXiv e-prints
Cen R., Chisari N. E., 2011, ApJ, 731, 11
Cen R., Ostriker J. P., 1999, ApJ, 514, 1
Cho J., 2014, ApJ, 797, 133
Corasaniti P. S., Ettori S., Rasera Y., Sereno M., Amodeo S., Breton M.-A., Ghirardini V., Eckert D., 2018, ApJ, 862, 40
Cucchetti E. et al., 2018, A&A, 620, A173
Davé R. et al., 2001, ApJ, 552, 473
de Graaff A., Cai Y.-C., Heymans C., Peacock J. A., 2017, ArXiv e-prints
Dedner A., Kemm F., Kröner D., Munz C.-D., Schnitzer T., Wesenberg M., 2002, Journal of Computational Physics, 175, 645
Eckert D. et al., 2019, A&A, 621, A40
Eckert D. et al., 2015, Nature, 528, 105
Eckert D., Molendi S., Vazza F., Ettori S., Paltani S., 2013, A&A, 551, A22
Ettori S. et al., 2019, A&A, 621, A39
Farnsworth D., Rudnick L., Brown S., Brunetti G., 2013, ApJ, 779, 189
Gheller C., Vazza F., Brüggen M., Alpaslan M., Holwerda B. W., Hopkins A. M., Liske J., 2016, MNRAS, 462, 448
Ghirardini V. et al., 2019, A&A, 621, A41
Giovannini G., Bonafede A., Feretti L., Govoni F., Murgia M., 2010, A&A, 511, L5
Hickox R. C., Markevitch M., 2007, ApJ, 671, 1523
Hoeft M., Brüggen M., 2007, MNRAS, 375, 77
Iapichino L., Schmidt W., Niemeyer J. C., Merklein J., 2011, MNRAS, 414, 2297
Kang H., Ryu D., Jones T. W., 2012, ApJ, 756, 97
Keshet U., Waxman E., Loeb A., 2004, ApJ, 617, 281
Khabibullin I., Churazov E., 2019, MNRAS, 482, 4972
Kolodzig A., Gilfanov M., Hütsi G., Sunyaev R., 2018, MNRAS, 473, 4653
Locatelli N., Vazza F., Domínguez-Fernández P., 2018, Galaxies, 6, 128
Loi F., Murgia M., Govoni F., Vacca V., Prandoni I., Bonafede A., Feretti L., 2019, MNRAS
Lotti S. et al., 2014, A&A, 569, A54
Lotti S., Mineo T., Jacquey C., Molendi S., D'Andrea M., Macculi C., Piro L., 2017, Experimental Astronomy, 44, 371
Martizzi D. et al., 2018, arXiv e-prints
McCammon D. et al., 2002, ApJ, 576, 188
Mernier F. et al., 2018, Space Sci. Rev., 214, 129
Nagai D., Lau E. T., 2011, ApJ, 731, L10
Nevalainen J. et al., 2015, A&A, 583, A142
Nicastro F. et al., 2018, Nature, 558, 406
Nicastro F., Krongold Y., Fields D., Conciatore M. L., Zappacosta L., Elvis M., Mathur S., Papadakis I., 2010, ApJ, 715, 854
O'Sullivan S. P. et al., 2018, ArXiv e-prints
Pfrommer C., Springel V., Enßlin T. A., Jubelgas M., 2006, MNRAS, 367, 113
Pinzke A., Oh S. P., Pfrommer C., 2013, MNRAS, 435, 1061
Piro L. et al., 2009, Experimental Astronomy, 23, 67
Planck Collaboration et al., 2013, A&A, 550, A134
Planelles S., Mimica P., Quilis V., Cuesta-Martínez C., 2018, MNRAS, 476, 4629
Roncarelli M., Cappelluti N., Borgani S., Branchini E., Moscardini L., 2012, MNRAS, 424, 1012
Roncarelli M., Ettori S., Dolag K., Moscardini L., Borgani S., Murante G., 2006a, MNRAS, 373, 1339
Roncarelli M. et al., 2018, A&A, 618, A39
Roncarelli M., Moscardini L., Tozzi P., Borgani S., Cheng L. M., Diaferio A., Dolag K., Murante G., 2006b, MNRAS, 368, 74
Roncarelli M., Pointecouteau E., Giard M., Montier L., Pello R., 2010, A&A, 512, A20
Ryu D., Kang H., Hallman E., Jones T. W., 2003, ApJ, 593, 599
Schmid C., Smith R., Wilms J., 2013, SIMPUT - A File Format for Simulation Input. Tech. report, HEASARC, Cambridge (MA)
Sheth R., Tormen G., 1999, MNRAS, 308, 119
Simionescu A. et al., 2011, Science, 331, 1576
Smith R. K., Brickhouse N. S., Liedahl D. A., Raymond J. C., 2001, ApJ, 556, L91
Sugawara Y., Takizawa M., Itahana M., Akamatsu H., Fujita Y., Ohashi T., Ishisaki Y., 2017, PASJ, 69, 93
Takei Y. et al., 2011, ApJ, 734, 91
Tanimura H., Aghanim N., Douspis M., Beelen A., Bonjean V., 2018, ArXiv e-prints
Urban O., Werner N., Simionescu A., Allen S. W., Böhringer H., 2011, MNRAS, 414, 2101
Ursino E., Branchini E., Galeazzi M., Marulli F., Moscardini L., Piro L., Roncarelli M., Takei Y., 2011, MNRAS, 414, 2970
Ursino E., Galeazzi M., Roncarelli M., 2010, ApJ, 721, 46
Vacca V. et al., 2018, MNRAS
van Weeren R. J., de Gasperin F., Akamatsu H., Brüggen M., Feretti L., Kang H., Stroe A., Zandanel F., 2019, arXiv e-

prints
van Weeren R. J. et al., 2016, ApJS, 223, 2
Vazza F., Brüggen M., Gheller C., 2013, MNRAS, 428, 2366
Vazza F., Brüggen M., Gheller C., Hackstein S., Wittor D., Hinz P. M., 2017a, Classical and Quantum Gravity, 34, 234001
Vazza F., Brüggen M., Hinz P. M., Wittor D., Locatelli N., Gheller C., 2018a, MNRAS, 480, 3907
Vazza F., Brunetti G., Brüggen M., Bonafede A., 2018b, MNRAS, 474, 1672
Vazza F., Brunetti G., Gheller C., 2009, MNRAS, 395, 1333
Vazza F., Dolag K., Ryu D., Brunetti G., Gheller C., Kang H., Pfrommer C., 2011, MNRAS, 418, 960
Vazza F., Ferrari C., Bonafede A., Brüggen M., Gheller C., Braun R., Brown S., 2015a, ArXiv e-prints
Vazza F., Ferrari C., Brüggen M., Bonafede A., Gheller C., Wang P., 2015b, A&A, 580, A119
Vazza F., Jones T. W., Brüggen M., Brunetti G., Gheller C., Porter D., Ryu D., 2017b, MNRAS, 464, 210
Wang P., Abel T., Kaehler R., 2010, New A, 15, 581
Werner N., Finoguenov A., Kaastra J. S., Simionescu A., Dietrich J. P., Vink J., Böhringer H., 2008, A&A, 482, L29
Wittor D., Vazza F., Brüggen M., 2017, MNRAS, 464, 4448
Zhuravleva I. V., Churazov E. M., Sazonov S. Y., Sunyaev R. A., Dolag K., 2011, Astronomy Letters, 37, 141